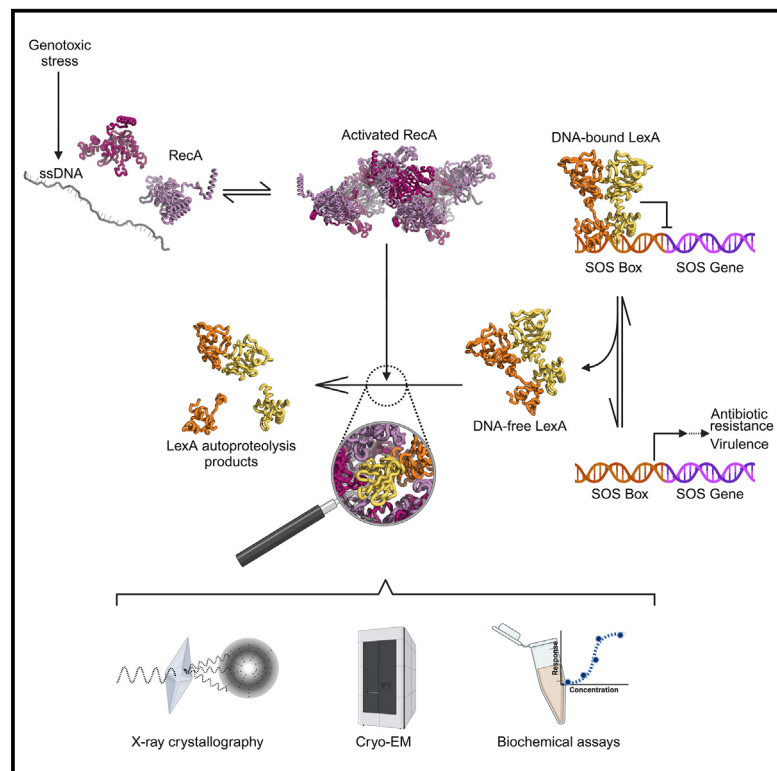**Article**

Snapshots of *Pseudomonas aeruginosa* SOS response reveal structural requisites for LexA autoproteolysis

Graphical abstract

Authors

Filippo Vascon, Sofia De Felice, Matteo Gasparotto, ..., Lorenzo Maso, Arjen J. Jakobi, Laura Cendron

Correspondence

laura.cendron@unipd.it

In brief

Natural sciences; Biological sciences; Microbiology; Biophysics

Highlights

- *P. aeruginosa* RecA and LexA were characterized by X-ray crystallography and cryo-EM

- RecA$_{Pa}$-LexA$_{Pa}$ complex structure reveals that binding stabilizes LexA$_{Pa}$ closed conformation

- Fluorescence polarization assays determined binding affinities of SOS complex members

- Peculiarities of the *P. aeruginosa* SOS complex can guide the design of specific inhibitors

CellPress

iScience

Article

Snapshots of *Pseudomonas aeruginosa* SOS response reveal structural requisites for LexA autoproteolysis

Filippo Vascon,[1,8] Sofia De Felice,[1,8] Matteo Gasparotto,[1,2] Stefan T. Huber,[3] Claudio Catalano,[4] Monica Chinellato,[1,5] Riccardo Mezzetti,[1] Alessandro Grinzato,[1,6] Francesco Filippini,[1] Lorenzo Maso,[1,7] Arjen J. Jakobi,[3] and Laura Cendron[1,9,*]

[1]Department of Biology, University of Padua, Via Ugo Bassi 58/b, 35131 Padova, Italy
[2]Department of Translational Brain Research, Central Institute of Mental Health (ZI), University of Heidelberg/Medical Faculty Mannheim, 68159 Mannheim, Germany
[3]Department of Bionanoscience, Kavli Institute of Nanoscience, Delft University of Technology, 2628CD Delft, the Netherlands
[4]NanoImaging Services, 4940 Carroll Canyon Road, Suite 115, San Diego, CA 92121, USA
[5]Department of Medicine, University of Padua, Via Giustiniani 2, 35121 Padova, Italy
[6]CM01 Beamline, European Synchrotron Radiation Facility (ESRF), Grenoble, France
[7]Aethon Therapeutics, Long Island City, NY 11101, USA
[8]These authors contributed equally
[9]Lead contact
*Correspondence: laura.cendron@unipd.it
https://doi.org/10.1016/j.isci.2024.111726

SUMMARY

Antimicrobial resistance poses a severe threat to human health and *Pseudomonas aeruginosa* stands out among the pathogens responsible for this emergency. The SOS response to DNA damage is crucial in bacterial evolution, influencing resistance development and adaptability in challenging environments, especially under antibiotic exposure. Recombinase A (RecA) and the transcriptional repressor LexA are the key players that orchestrate this process, determining either the silencing or the active transcription of the genes under their control. By integrating state-of-the-art structural approaches with *in vitro* binding and functional assays, we elucidated the molecular events activating the SOS response in *P. aeruginosa*, focusing on the RecA-LexA interaction. Our findings identify the conserved determinants and strength of the interactions that allow RecA to trigger LexA autocleavage and inactivation. These results provide the groundwork for designing novel antimicrobial strategies and exploring the potential translation of *Escherichia coli*-derived approaches, to address the implications of *P. aeruginosa* infections.

INTRODUCTION

To guide and coordinate the development of novel antimicrobial strategies, several national and international health agencies constantly monitor the prevalence of antibiotic-resistant bacterial pathogens, prioritizing those representing the greatest threats.[1,2] The gram-negative bacterium *Pseudomonas aeruginosa* always finds its spot in these "priority lists", as it displays a vast spectrum of antibiotic resistance mechanisms[3] and a high frequency of infections among hospitalized patients, either as a direct etiologic agent or as a comorbidity, occasionally acquired in the healthcare settings.[4] Indeed, as an opportunistic pathogen, *P. aeruginosa* mainly infects patients suffering from immune deficiencies, severe wounds, and pulmonary diseases, including cystic fibrosis and COVID-19.[5,6]

Together with multi-drug resistance, a notable variety of virulence factors determines *P. aeruginosa* pathogenicity and recalcitrance. Several surface appendages (pili) and proteins (e.g., lectins) mediate *P. aeruginosa* adhesion to the host tissues,[3,5]

while secreted proteases and toxins damage the host's tissue components, immune defenses and physiological functions.[5,6] *P. aeruginosa* is known to form biofilms and communicate via quorum sensing (QS). These interwoven features are of great relevance in the fight against bacterial pathogens, since biofilms physically shield the enclosed sensitive cells from the action of antimicrobials and favor the differentiation of persister sub-populations,[3,7] while QS regulates the expression of virulence factors.[6]

In recent years, anti-evolutive, anti-virulence, anti-biofilm, and quorum quencher strategies have been proposed as new approaches in antimicrobial chemotherapy, as they could counteract the rapid acquisition of antibiotic resistance and weaken the pathogenicity of bacterial infections.[8–11]

The SOS response pathway represents a master regulator involved in the control of cell division, fitness to environmental stressors, prophage activation, biofilm maturation, production of virulence factors, and error-prone DNA replication.[12–15] Most importantly, it is the most conserved mechanism of

bacterial response to DNA damage induced by exposure to antimicrobials, UV radiation, and reactive oxygen species. Because of these reasons, it is regarded as one of the best targets of anti-evolutive and antivirulence therapies.[9,10,16]

The plethora of SOS-regulated mechanisms is species-specific and depends on the set of genes (the *SOS regulon*) controlled by the master SOS transcriptional repressor LexA through its binding to specific operator sequences in the promoter region of SOS genes (*SOS boxes*).[17]

A prerequisite for triggering the SOS response is the activation of recombinase A (RecA), which senses single-stranded DNA generated by the genotoxic damage and oligomerizes on it in an ATP-dependent manner. RecA oligomers promote the autoproteolytic cleavage of the dimeric LexA, in its DNA-free form.[18] This activity is exerted by a Ser/Lys dyad (S125/K162 in *P. aeruginosa*) on a *scissile* peptide bond (A90-G91 in *P. aeruginosa*) located on a flexible loop, which can switch between an inactive (open) and a prone-to-cleavage (closed) conformation.[19,20]

The autoproteolysis event hinders the transcriptional repressor activity of the cleavage products (*i.e.*, LexA N-terminal and C-terminal domains, NTD and CTD) and shifts the equilibrium between the DNA-bound and unbound LexA toward the latter state. LexA autoproteolysis thus leads to the active expression of the SOS genes, with tightly regulated expression levels, chronological order, and duration that depend on LexA affinity and binding kinetics on the different SOS boxes.[17,21]

Despite the species-specificity of the SOS regulon—e.g., it accounts for 57 genes in *E. coli*,[22] 33 genes in *Bacillus subtilis*, 48 genes in *Salmonella enterica*,[23] and 15 genes in *P. aeruginosa*[24]—it invariably includes factors involved in DNA repair, in particular error-prone translesion (TLS) DNA polymerases.[25] Despite less studied than the SOS-regulated *Pol II*, *Pol IV*, and *Pol V* of *E. coli*, other error-prone DNA polymerases (ImuB and ImuC, also known as DnaE2) encoded by SOS-inducible *imuA-imuB-dnaE2* gene cassettes are broadly distributed among bacterial taxa, including *P. aeruginosa*,[25–27] confirming the centrality of translesion synthesis in the general SOS response. These TLS polymerases can bypass DNA lesions otherwise incompatible with replicative polymerases, at the cost of high error rates, thus introducing mutations.[28] As a result, one of the primary outcomes of the SOS response is a transient hypermutator state that promotes genetic diversity, adaptive mutation and the evolution of antimicrobial resistance. Given its importance for the acquisition of antimicrobial resistance and its high conservation, the SOS response is currently receiving attention as a target of antibiotic-adjunctive therapies, which might prolong antibiotics effectiveness and even increase their efficacy.[29–35]

While the structural features of the single components LexA and RecA have been determined by X-ray crystallography or cryogenic electron microscopy (cryo-EM), a substantial lack of structural and mechanistic knowledge about the SOS complex has limited our comprehension of the stimulatory role played by RecA toward LexA autocleavage. Only recently, cryo-EM studies on the SOS complex of *E. coli* began to shed light on the interaction site of either LexA C-terminal domain or full-length protein with RecA/ssDNA/ATPγS oligomers.[36,37]

The cascade of events promoted by DNA damage in *P. aeruginosa* (Pa) still needs a complete characterization, and several recent works have unveiled a previously unknown complexity compared to the well-studied *E. coli* (Ec) model (e.g., multiple LexA-like transcriptional regulators and interconnections with other stress-response pathways[38–41]). Deepening our understanding of the principal protein actors of *P. aeruginosa* SOS response is necessary to determine to which extent the anti-SOS approaches developed in *E. coli* could be translated to this pathogen.

With this aim, our work investigated the core of the SOS response in *P. aeruginosa*, obtaining the structures of the isolated components (LexA$_{Pa}$ C-terminal domain and RecA$_{Pa}$/ssDNA/ATPγS), as well as the cryo-EM structure of the activation complex (LexA$_{Pa}$S125A-RecA$_{Pa}$/ssDNA/ATPγS assembly). Our structural data, integrated by experimental measurements of the affinity of the binding partners and proteolysis assays, let us describe the molecular events governing the binding and activation of the SOS response players in this health-threatening pathogen.

RESULTS

Crystal structure of LexA$_{Pa}$^{CTD} G91D

Two mutants of *P. aeruginosa* LexA were expressed in *E. coli*, purified by affinity chromatography, and used for the structural studies described in this work, which require a stable LexA variant unable to undergo RecA*-dependent or independent autoproteolysis. Specifically, the LexA$_{Pa}$S125A mutant consists of the full-length protein carrying the S125A mutation in the catalytic dyad. Conversely, LexA$_{Pa}$^{CTD} G91D comprises only the LexA$_{Pa}$ C-terminal domain (CTD, from Gly81 to Arg204) bearing an inactivating mutation on the cleavage site. While the former will be used to study the RecA$_{Pa}$-LexA$_{Pa}$ interaction (as reported in the further section), the latter is more amenable to protein crystallization as it lacks the flexible linker and NTD.

In agreement with previous observations,[42] analytical size exclusion chromatography showed that both proteins behave as homodimers in solution (Figure 1A). Specifically, LexA$_{Pa}$ S125A was eluted with an apparent molecular weight of 62 ± 6 kDa, and LexA$_{Pa}$^{CTD} G91D eluted at an apparent molecular weight of 35 ± 4 kDa, in both cases corresponding to roughly double the expected molecular weight of the monomeric forms (24 kDa and 14 kDa, respectively). Moreover, SDS-PAGE-based analysis of RecA$_{Pa}$/ssDNA/ATPγS (RecA$_{Pa}$*)-induced autoproteolysis reactions revealed similar self-cleavage kinetics for wild-type full-length LexA$_{Pa}$ and LexA$_{Pa}$^{CTD}, while both the S125A and G91D mutations completely abated the catalytic activity of the LexA$_{Pa}$ variants (Figures 1B and S1E). These observations confirmed that the C-terminal domain provides all the determinants for LexA homodimerization and autoproteolysis.

The structure of LexA$_{Pa}$^{CTD} G91D has been resolved by X-ray macromolecular crystallography at 1.70 Å resolution (PDB: 8B0V; statistics in Table S1). Two independent molecules of LexA$_{Pa}$^{CTD} G91D define the asymmetric unit and are fully visible from residue Gly81 to Arg204, while the functional homodimer can be reconstructed by applying a crystallographic symmetry
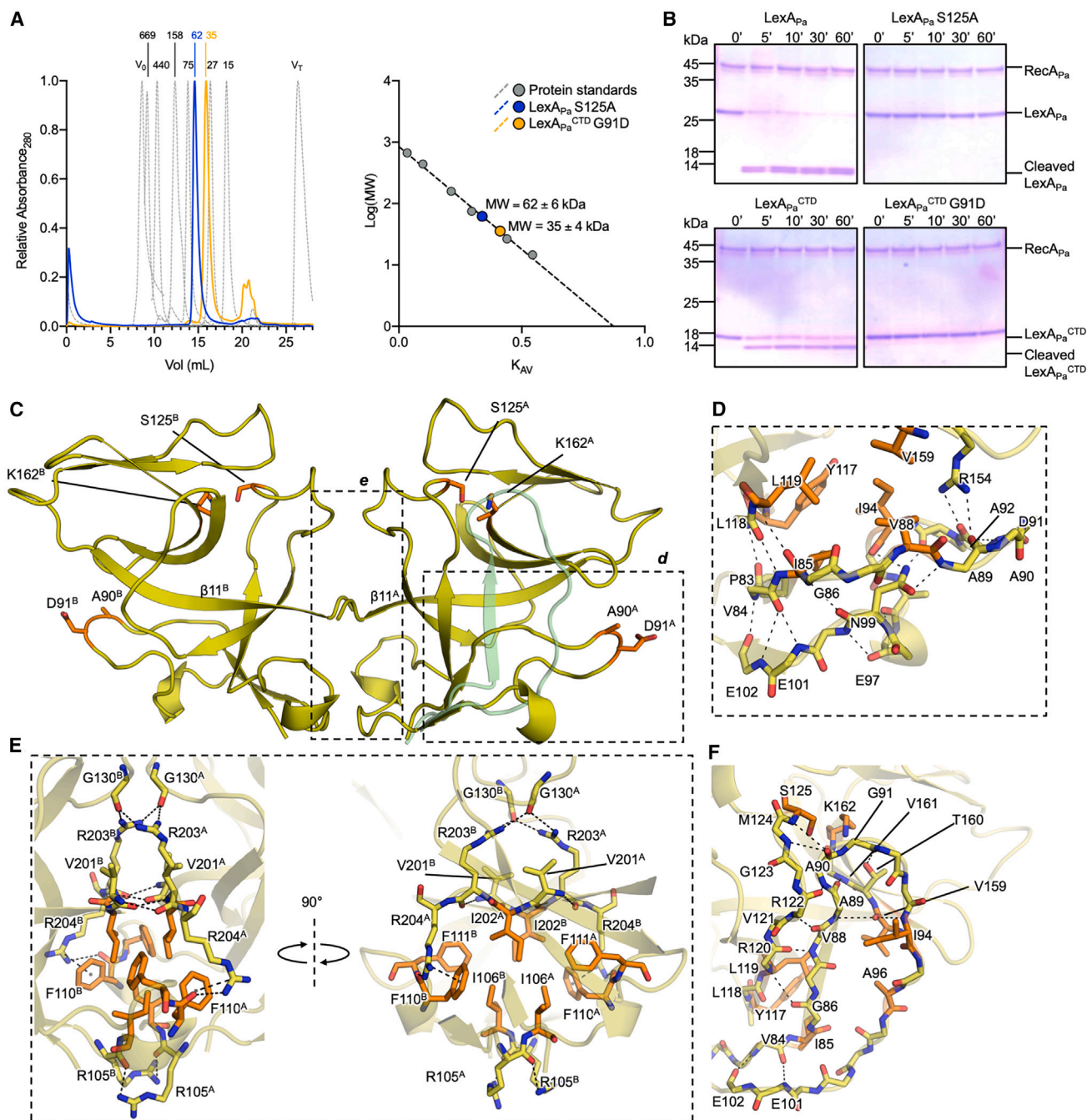
Figure 1. Structural analysis of LexA$_{Pa}^{CTD}$

(A) Analytical size exclusion chromatography of LexA$_{Pa}$S125A (blue) and LexA$_{Pa}^{CTD}$G91D (yellow; chromatograms on the left and standard curve interpolation on the right).

(B) SDS-PAGE-based RecA$_{Pa}$*-induced autoproteolysis assay of 4 LexA$_{Pa}$ variants: full-length LexA$_{Pa}$, either wt or S125A inactive mutant, and LexA$_{Pa}^{CTD}$, either wt or G91D uncleavable mutant. One representative gel is shown, see also Figure S1E for band quantification.

(C) Overall view of the LexA$_{Pa}^{CTD}$G91D dimer (chains A and B), as revealed by X-ray crystallography. The catalytic dyad (S125/K162) and the mutated self-cleavage site (A90-D91) of each monomer are shown as orange sticks. Boxed regions are zoomed in panels D and E. Superposed (transparent green cartoon) is the closed conformation of LexA$_{Pa}$ cleavable loop found in LexA$_{Pa}$S125A bound to RecA$_{Pa}$*.

(D) Detailed view of the cleavable loop (chain A) in the "open" (inactive) conformation. Hydrogen bonds engaging the residues of the loop are represented as dashed lines, while residues involved in a hydrophobic cluster are depicted as orange sticks.

(legend continued on next page)

operator and is hereafter referred to as chains A and B (indicated as superscript; Figure 1C).

Electron densities that could not be assigned either to protein or ordered solvent have been interpreted as two calcium cations, two MES molecules, and three ethylene glycol molecules, all components of the crystallization conditions and not involved in any functional contact with the protein. A few weak electron densities remain uninterpreted and may be due to traces of the Tb-Xo4 nucleating agent[43,44] used in the crystallization process.

The homodimerization of LexA$_{Pa}$^{CTD} G91D is mainly driven by the antiparallel pairing of the C-terminal portion of the β11 strands (secondary structures are numbered in Figure S1A) of the interacting protomers (Figures 1C and 1E). More in detail, Val201^A backbone oxygen and nitrogen are hydrogen bonded to Arg203^B nitrogen and oxygen, respectively. Other hydrogen bonds are established between Arg203^A-NH1 and Gly130^B-O, Arg204^A-NH1 and Phe110^B-O, Arg105^A-NH1 and Arg105^B-O. The sidechain of Arg204^A forms a cation-π interaction with the aromatic ring of Phe110^B. Since all these interactions are mutual, they appear twice at the interaction surface. The core of LexA$_{Pa}$^{CTD} G91D homodimerization surface is further stabilized by a hydrophobic cluster involving Ile106, Phe110, Phe111, and Ile202 of each chain (Figure 1E).

The cleavage loop (residues 81–103) of both LexA$_{Pa}$^{CTD} G91D chains is in the inactive "open" conformation, with the mutated cleavage site (Ala90-Asp91) distant from the catalytic pocket that hosts the dyad Ser125/Lys162. This conformation is similar to those assumed by previously crystallized LexA^{CTD} mutants from other bacterial species (e.g., PDB: 1JHF, 3JSP, 3K2Z).

In the "open" conformation, the base of the cleavage loop (Pro83-Ile85) is structured as a β-strand and pairs parallel to the β-strand Leu118-Arg120 (three intrachain hydrogen bonds are established between the backbone atoms; Figure 1D). The other extremity of the loop (Ile100-Cys104) assumes a β-sheet structure as well, and pairs in an antiparallel fashion with the aforementioned strands. On the tip of the loop, the backbone oxygen atoms of Ala89 and Ala92 are hydrogen bonded to the η nitrogen atoms of Arg154, while Ile94 is buried among Val88, Ile85, Leu119, Tyr117, Val159, and Glu195, forming several hydrophobic interactions.

The conformation of LexA$_{Pa}$^{CTD} G91D cleavable loop was compared to that of LexA$_{Pa}$S125A, subsequently obtained by cryo-EM in complex with RecA$_{Pa}$* (see the section "cryo-EM structure of the RecA$_{Pa}$*-LexA$_{Pa}$ complex"; Figure 1C). The latter is in the active "closed" conformation (analogous to the one observed in PDB: 1JHE, 3JSO, 8GMS, and 8TRG), with the cleavage site buried inside the catalytic pocket. In this form, the β-strand that precedes the cleavage site extends until Ala90, increasing the number of interactions with the other core β-strands. Notably, in this conformation, Ile94 becomes solvent-exposed, opening the hydrophobic pocket where it was hosted in the open state (Figure 1F).

The sequence of LexA$_{Pa}$ shows a high degree of identity with that of *E. coli* LexA (LexA$_{Ec}$; 64% identity; Figure S1A). As a consequence, LexA$_{Pa}$^{CTD} G91D has a highly conserved structural arrangement compared to LexA$_{Ec}$ (Figure S1B; RMSD of 0.98 Å between LexA$_{Pa}$^{CTD} G91D and PDB: 1JHF, calculated over 124 pairs of α-carbon atoms by Gesamt[45]). However, LexA$_{Pa}$ displays a shorter C-terminal tail and a longer linker region between its CTD and NTD than LexA$_{Ec}$ and these differences should be considered in the rational design of potential inhibitors of LexA$_{Pa}$.

Cryo-EM structure of RecA$_{Pa}$*

RecA$_{Pa}$ was expressed in *E. coli* and purified by affinity chromatography. To assemble the active nucleoprotein complex, RecA$_{Pa}$ was co-incubated with 72mer oligo(dT) ssDNA and the slowly hydrolysable adenine nucleotide ATPγS. The desired RecA$_{Pa}$* oligomers were stabilized by chemical crosslinking and isolated by size exclusion chromatography before vitrification of samples for cryo-EM analysis.

The cryo-EM structure of RecA$_{Pa}$* was obtained by helical reconstruction, at a global resolution of 4.2 Å (Figures 2A, S2, and S3; Table S2; PDB: 8S70, EMD-19761). The final RecA$_{Pa}$* model is organized as a right-handed helix described by a twist of 59.2°, a rise of 15.4 Å, six RecA$_{Pa}$ protomers per turn (corresponding to a pitch of 92.5 Å), and an average diameter of ~110 Å (Figures 2B–2D and S3), similar to that reported for the *E. coli* homolog.[36,37,46,47] This arrangement shows the features of RecA/ssDNA filaments in the ATP-bound extended form.[48,49] The density allowed the assignment of residues 1–328, and the identification of the contact sites with ssDNA and ATPγS (Figures 2E–2G).

Each RecA$_{Pa}$ protomer interacts with the ssDNA filament by the central core domain (including seven α-helices and seven β-strands), from which the N- and C-terminal domains protrude. The N-terminal domain is constituted by a long α-helix and a flexible loop, while the C-terminal domain is mainly composed of three α-helices (α9-α11) and an intervening three-stranded β-sheet (β12-β14). The ssDNA, which lies close to the central axis and wraps around it, is contacted by RecA$_{Pa}$ "ventral" L1 and L2 loops (residues 156–164 and 194–213; Figures 2E and S1C). The N-terminal helix of one RecA$_{Pa}$ protomer ("*n+1*") points toward the 5′ termini of ssDNA filament and docks on the "dorsal" part of the adjacent RecA$_{Pa}$ monomer ("*n*"; Figure 2E), interacting with the α-helix 120–134 residues mainly by the formation of a cluster of hydrophobic residues (Leu114, Ile127, Leu131, and Val137 of RecA$_{Pa}$^{n} and Leu9, Leu13, Ile16, Phe20, and Val25 of RecA$_{Pa}$$^{n+1}$). An average surface area of 2047 Å^2 is buried on each RecA$_{Pa}$ protomer at the interface with each of its neighboring ones, potentially establishing multiple van der Waals contacts and H-bonds.

One ATPγS molecule is coordinated at the interface between two RecA$_{Pa}$ protomers (Figure 2G). Given the limited resolution

---

(E) Detailed views of the homodimerization surface of LexA$_{Pa}$^{CTD}. Dashed lines indicate H-bonds, salt bridges and cation-π interactions, while residues involved in a hydrophobic cluster are depicted as orange sticks.

(F) LexA$_{Pa}$ cleavable loop in the "closed" (active) conformation. Dashed lines indicate H-bonds stabilizing the loop in this state, while orange sticks correspond to the catalytic dyad and to the hydrophobic residues indicated in panel B. The movement of the loop brings the cleavage site inside the catalytic pocket and at the same time opens a hydrophobic cavity (Y117, L119, V159, I85) that hosts I94 in the open conformation.
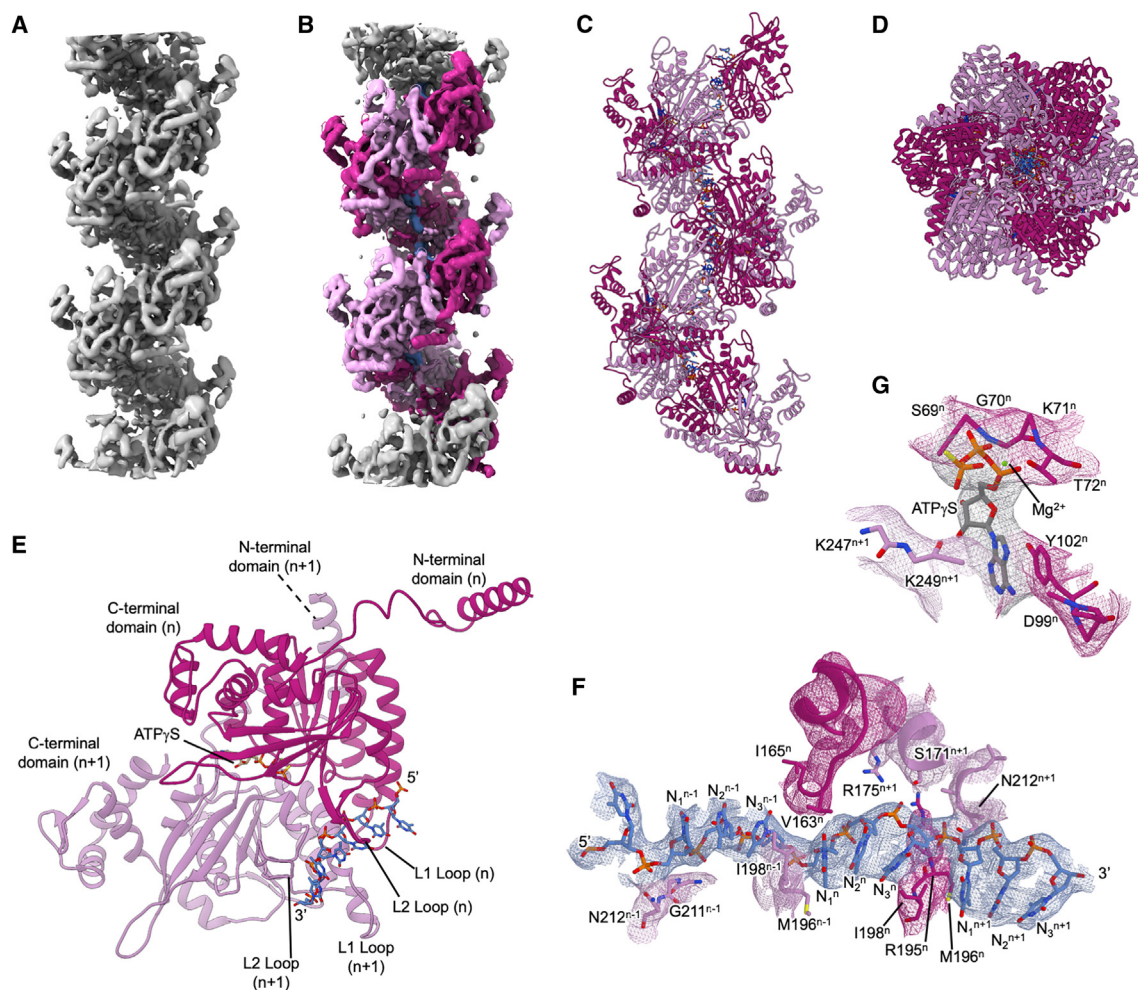
Figure 2. Cryo-EM structure of RecA$_{Pa}$*

(A) RecA$_{Pa}$* cryo-EM density map.

(B–D) Coloring of density regions corresponding to RecA$_{Pa}$* protomers and (C and D) zoom on the atomic model (two perpendicular views).

(E) Zoom on two adjacent RecA$_{Pa}$* protomers assembled on ssDNA (RecA$_{Pa}^{n}$ and RecA$_{Pa}^{n+1}$, moving from 5′ to 3′ on ssDNA). Detailed views of the cryo-EM map around ssDNA (F) and ATPγS (G), and RecA$_{Pa}$ residues interacting with them.

of our maps, we can only speculate about the main interactions that this nucleotide might establish, by comparing the nucleotide-binding pocket to previous structures of RecA$_{Ec}$* oligomers obtained at higher resolution (PDB: 7JY6 and 3CMW).[46,47] ATPγS phosphate groups coordinate a Mg^{2+} cation, which in turn is kept in place by the side chain of Thr72 of RecA$_{Pa}^{n}$ (Figure 2G). The phosphate moieties are stabilized by hydrogen bonds with the backbone atoms of residues 68–73 of RecA$_{Pa}^{n}$, and by salt bridges with the side chains of Lys71^{n}, Lys247^{n+1}, and Lys249^{n+1}. The adenine base might interact with acidic residues Asp99 of RecA$_{Pa}^{n}$, Asp249, and Glu250 of RecA$_{Pa}^{n+1}$ and can be further stabilized by interacting with Tyr102^{n}.

When RecA$_{Pa}$ is complexed with ssDNA, each RecA$_{Pa}$ protomer spans mainly three nucleotides (5′-N$_1$-N$_2$-N$_3$-3′; Figure 2F) but further contacts the phosphates of one nucleotide upstream (N$_3^{-1}$) and one nucleotide downstream (N$_1^{+1}$) of the primarily engaged triplet (Figure 2F). A physical torsion can be observed

between nucleotides N$_3$ and N$_1^{+1}$ (or, equivalently but in the opposite direction, between N$_1$ and N$_3^{-1}$), with the side chain of Ile198^{n} inserting between their nucleobases. The phosphate group of N$_1$ is at H-bond distance to RecA$_{Pa}^{n}$ Asn212 and Met196^{n-1}, while the phosphate of N$_2$ interacts with the backbone nitrogen atoms of Gly210^{n} and Gly211^{n}. The negatively charged phosphate group of N$_3$ could contact the side chains of Arg195^{n} and Arg175^{n+1}, as well as Thr209^{n} and Ser171^{n+1}. These interactions are encountered periodically along the RecA$_{Pa}$* filament as they are established with the backbone of the DNA strand. Other local electrostatic or hydrophobic contacts with nucleobases depend on the nucleotide sequence.

RecA$_{Pa}$ is highly similar to *E. coli* RecA (RecA$_{Ec}$) in terms of both sequence (71% identity; Figure S1C) and structure (RMSD of 1.06 Å between RecA$_{Pa}$ chain F and PDB 7JY6 chain F, calculated over 320 pairs of α-carbon atoms by Gesamt; Figure S1D), with the highest local differences affecting the
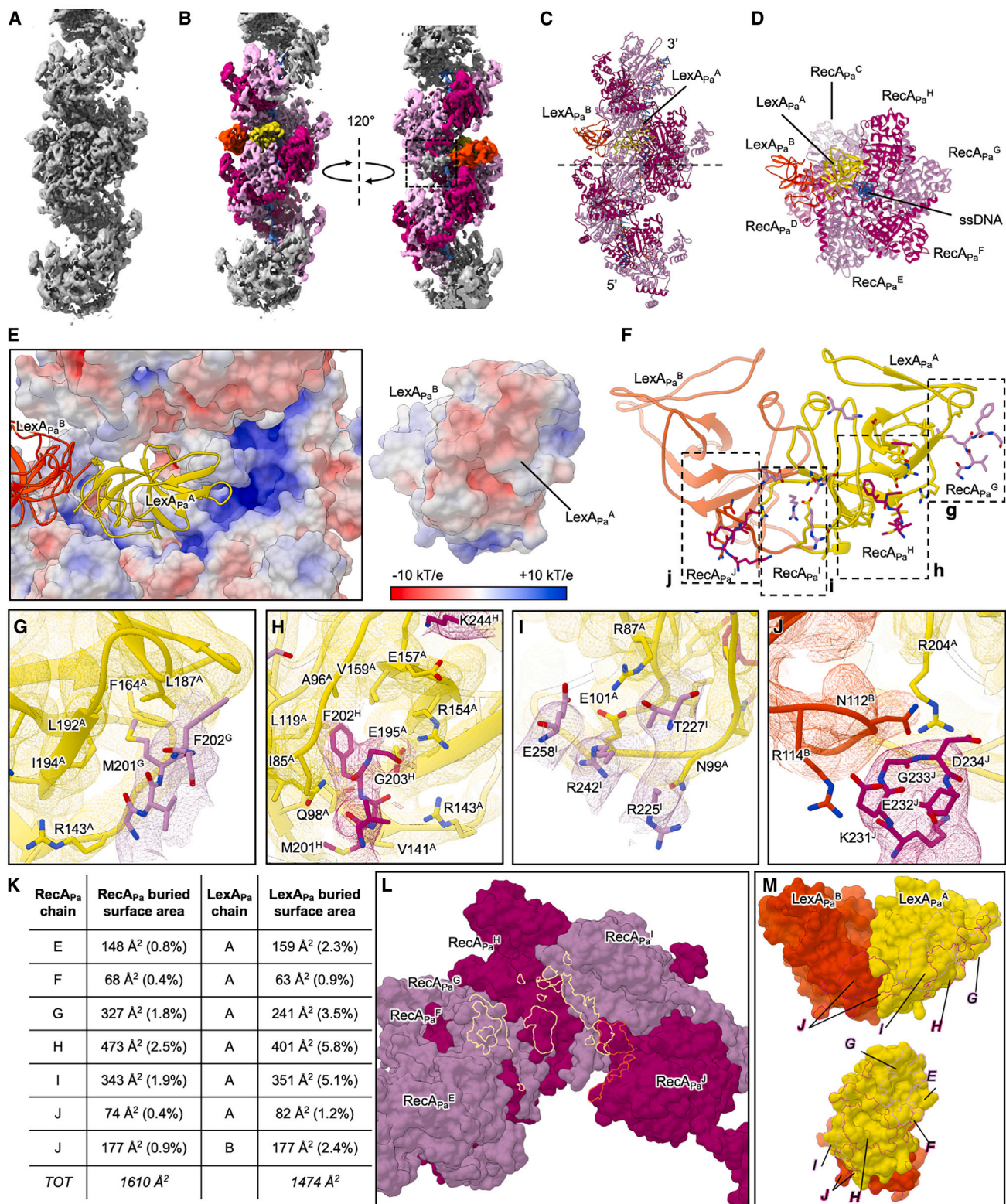
(legend on next page)

C-terminal domain (residues 280–328), and the "ventral" loops (residues 159–165, 199–203, and 231–235).

Cryo-EM structure of the RecA$_{Pa}$*-LexA$_{Pa}$ complex

To gain insights into the interaction between RecA$_{Pa}$* (RecA$_{Pa}$/ssDNA/ATPγS) and LexA$_{Pa}$, the two interactors were co-incubated, chemically crosslinked, and the desired complexes were isolated by size exclusion chromatography for subsequent cryo-EM studies. Since the interaction of LexA with RecA* triggers LexA autoproteolysis, to identify its docking site onto RecA$_{Pa}$* but preventing hydrolysis occurrence, the LexA$_{Pa}$S125A non-cleavable mutant was used to form the complex.

The structure of RecA$_{Pa}$* in complex with LexA$_{Pa}$S125A was determined by cryo-EM at an overall resolution of 3.4 Å (Figures 3A and S2–S4; Table S2; PDB: 8S7G, EMD-19771). The density of the LexA$_{Pa}$ dimer is visible inside the helical groove of the RecA$_{Pa}$/ssDNA filament (Figure 3B). Interestingly, only the C-terminal domains (residues 81–204) of both LexA subunits were traceable in the maps, while the N-terminal DNA binding domains were largely undefined. A blurred extra density at low resolution (>7 Å) is observed protruding from the LexA$_{Pa}^{CTD}$ dimer. Although we cannot rule out the possibility that it derives from residual traces of map averaging, its position and size suggest it corresponds to the LexA$_{Pa}$ NTD domain (Figures 3B and S4). Its poorly defined nature is probably due to intrinsic flexibility, supporting the notion that the main binding determinants are located on the C-terminal domains, where the autocleavage reaction occur.

Our data showed that full-length LexA$_{Pa}$ non-stoichiometrically occupies the RecA$_{Pa}$* helical groove and hence does not follow its helical symmetry (Figures 3B–3D). Indeed, the RecA$_{Pa}$*-LexA$_{Pa}$ complex could only be resolved by local refinement after dropping the helical symmetry assumption. The LexA$_{Pa}^{CTD}$ subunit deeply buried inside RecA$_{Pa}$* groove (chain A or LexA$_{Pa}^{A}$) is well defined in the maps and directly interacts with three consecutive protomers of RecA$_{Pa}$ (chains G, H, and I, assembled 3'-5' on ssDNA), contacting the L2 loops (residues 197–207) of two of them (G and H) and the core β-strands of the third (Figures 3E–3M). Conversely, chain B (LexA$_{Pa}^{B}$, which is slightly less well-defined in the map) keeps the LexA dimeric arrangement, but remains more peripheral, most likely establishing a few contacts only with RecA$_{Pa}$* chain J. The cleavable loop of LexA$_{Pa}$ chain A assumes the closed conformation, producing a hydrophobic cavity (defined by the residues Ile85, Ala96, Tyr117, Leu119, Leu137, Val139, Val152, Val159, and Glu195) that is explored by Phe202 of

RecA$_{Pa}$ chain H (Figure 3H). This complex architecture suggests that the L2 loop of RecA$_{Pa}^{H}$ (residues 202–204) is kept in place by a network of polar interactions established at the interface between RecA$_{Pa}^{H}$ Met201, Phe202 and Gly203 and side chains of LexA$_{Pa}^{A}$ Gln98, Arg143, Arg154, and Glu195. LexA$_{Pa}^{A}$ might establish additional contacts with the L2 loop of the upstream RecA$_{Pa}$ protomer in the helical assembly (RecA$_{Pa}^{G}$): in this case Met201 protrudes into a nearby hydrophobic pocket of LexA$_{Pa}^{A}$, defined by Leu187, Leu192, Phe164, and Ile194 (Figure 3G). LexA$_{Pa}$ chain B maintains its cleavable loop in the open state as in the X-ray structure of LexA$_{Pa}^{CTD}$ G91D described previously, with the "Phe202-binding" hydrophobic pocket made inaccessible by LexA$_{Pa}$ Ile94.

Analyzing the surface electrostatic potential of each member of the complex, the groove of RecA$_{Pa}$* oligomer (positively charged) and the interacting flank of LexA$_{Pa}^{A}$ in the cleavable conformation (negatively charged) display a wide and remarkable complementarity (Figure 3E). Even though the map resolution does not allow to clearly define the position of their side chains, electrostatic interactions are likely established between RecA$_{Pa}^{H}$ Lys244, RecA$_{Pa}^{I}$ Lys231, RecA$_{Pa}^{I}$ Arg242, RecA$_{Pa}^{I}$ Glu258 and RecA$_{Pa}^{J}$ Asp234 and LexA$_{Pa}^{A}$ Glu157, Glu158, Glu101, Arg87 and Arg204 (Figures 3I and 3J).

Fluorescence polarization-based analysis of RecA$_{Pa}$ affinity for its ligands

To characterize the binding affinity of RecA$_{Pa}$ for its ligands (ssDNA and ATPγS), a fluorescence polarization (FP)-based assay was set up using a fluorescein amidite (FAM)-labeled 32mer ssDNA filament and leveraging on the FP increase observed upon RecA$_{Pa}$ oligomerization on it.[50]

A first experiment (Figure 4A) was carried out by titrating ssDNA with RecA$_{Pa}$ in the presence of a large excess of ATPγS. The apparent affinity of RecA$_{Pa}$ for FAM-32mer ssDNA, resulting from data fitting with the Hill equation, lies in the nanomolar range ($K_D^{App} = 82 \pm 34$ nM) and the Hill coefficient suggests binding cooperativity ($h = 1.9 \pm 0.3$), as expected for RecA oligomerization on DNA.[51]

A second experiment (Figure 4B) was performed by keeping the concentration of FAM-32mer ssDNA and RecA$_{Pa}$ constant while increasing the concentration of ATPγS in the different samples. The obtained apparent K_D of RecA$_{Pa}$ for ATPγS in the presence of FAM-32mer ssDNA ($K_D^{App} = 2.0 \pm 0.2$ μM; $h > 1.5$) is about 5 times higher than the previously determined K_D of E. coli RecA for the same nucleotide[52] ($K_D < 0.4$ μM). Such differences might arise from structural peculiarities of E. coli and P. aeruginosa RecA ATP-binding sites or from

Figure 3. Cryo-EM structure of RecA$_{Pa}$*-LexA$_{Pa}$S125A

(A) Cryo-EM density map of the RecA$_{Pa}$-LexA$_{Pa}$S125A complex. The displayed map has been locally sharpened using LocScale2.

(B) Coloring of density regions corresponding to RecA$_{Pa}$* protomers (purple tones) and LexA$_{Pa}$ CTD chains A (yellow) and B (orange). The boxed region represents a low-resolution density, which was not interpreted by the atomic model and that might be due to the LexA$_{Pa}$ NTD.

(C and D) (C) Side and (D) front views of the RecA$_{Pa}$*-LexA$_{Pa}$S125A atomic model. The dashed line in panel C represents a virtual plane where the model was cut in panel D to allow LexA$_{Pa}$ clear visualization.

(E) Electrostatic surface potential of RecA$_{Pa}$* and LexA$_{Pa}^{CTD}$, showing complementarity on the interacting surfaces.

(F) LexA$_{Pa}^{CTD}$ dimer and the main binding determinants on four RecA$_{Pa}$ protomers (chains G–J), zoomed in panels (G–J).

(K) Details of the interfaces buried between LexA$_{Pa}$ and different RecA$_{Pa}$* protomers.

(L and M) The corresponding interacting surfaces are represented in panels (L) (on RecA$_{Pa}$* surface) and (M) (on LexA$_{Pa}$ surface, front and side views). Contour lines are colored as the interacting chain.
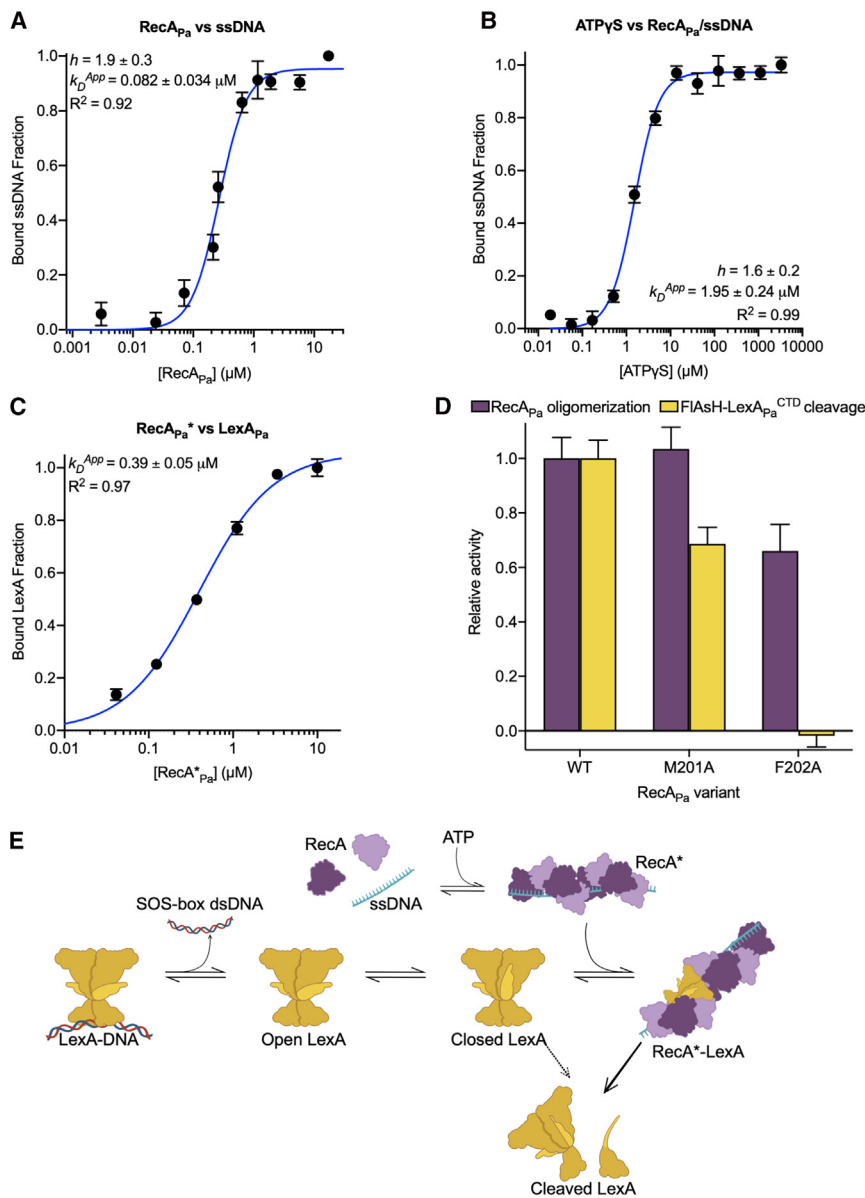
Figure 4. Analysis of RecA$_{Pa}$ interactions with its natural ligands (ATPγS, ssDNA and LexA$_{Pa}$)

(A–C) FP-based titrations of (A) FAM-32mer ssDNA with RecA$_{Pa}$ (ATPγS in molar excess), (B) RecA$_{Pa}$/FAM-32mer ssDNA with ATPγS and (C) FlAsH-LexA$_{Pa}$^{CTD}S125A with activated RecA$_{Pa}$ (RecA$_{Pa}$*, RecA$_{Pa}$/ssDNA/ATPγS). Points represent the average of three replicates while error bars represent standard errors of the mean (SEM).

(D) Relative activity of RecA$_{Pa}$ variants (wt, M201A, F202A) in terms of oligomerization on ssDNA and induction of FlAsH-LexA$_{Pa}$^{CTD} autoproteolysis. Bars represent averages of three replicates ±SEM. See also Figure S5 for time-course traces.

(E) Overview of the model proposed for the molecular process promoted by RecA$_{Pa}$*, that leads to the autocleavage of LexA$_{Pa}$. LexA$_{Pa}$ can bind RecA$_{Pa}$* if it is free from DNA and with the cleavable loop in the closed conformation. The binding to RecA$_{Pa}$* allows the self-cleavage of LexA$_{Pa}$, that otherwise is mainly prevented.

Investigations on the impact of F202 and M201 on RecA$_{Pa}$ activities

The cryo-EM structure of RecA$_{Pa}$*-LexA$_{Pa}$ showed that the main binding determinants for LexA$_{Pa}$ are located on the L2 loop of RecA$_{Pa}$, particularly on residues Met201 and Phe202. To assess the biological relevance of the cryo-EM structure of the SOS complex, we mutated these two amino acids to alanine, and we evaluated the impact of such mutations on RecA$_{Pa}$ co-protease activity on LexA$_{Pa}$. Previous studies pointed out that the L2 loop of RecA is crucial for its binding to ssDNA[53–56] (therefore for the formation of functional RecA* oligomers) and for homologous recombination.[46,57] As such, we investigated the effect of M201A and F202A mutations on RecA$_{Pa}$ oligomerization proficiency, as an impairment of this activity might result in a deficiency in co-proteolysis on LexA$_{Pa}$ independent from the disruption of any direct contacts with the latter.

Both activities (i.e., RecA$_{Pa}$ oligomerization on ssDNA and induction of LexA$_{Pa}$ autoproteolysis) were tested by FP-based assays. To study RecA$_{Pa}$ oligomerization on ssDNA, each variant of interest was incubated with the aforementioned FAM-32mer reporter under conditions close to saturation of ssDNA according to our previous experiments (10 nM FAM-32mer, 1 μM RecA$_{Pa}$, 10 μM ATPγS). Monitoring the FP signal on a 60-min timescale, we observed that the wild-type RecA$_{Pa}$ reached a plateau in roughly 18 min (Figure S5A).

RecA$_{Pa}$M201A exhibited filamentation kinetics similar to the wild type, while RecA$_{Pa}$F202A reached the steady-state plateau much more slowly. This resulted in approximately a 30% reduction in RecA$_{Pa}$F202A oligomerization compared to the wild type

limitations of the different experimental methods used. In particular, the biophysical assay reported here indirectly measures the affinity of RecA$_{Pa}$ for ATPγS, since it relies on RecA$_{Pa}$ oligomerization on the fluorescent reporter FAM-32mer ssDNA and on the influence that the nucleotide cofactor has on this interaction.

A different FP-based assay was employed to estimate the affinity of RecA$_{Pa}$* for LexA$_{Pa}$ (Figure 4C), titrating a fluorescently labeled and uncleavable variant of LexA$_{Pa}$ C-terminal domain (FlAsH-LexA$_{Pa}$^{CTD} S125A) with increasing concentrations of pre-activated RecA$_{Pa}$*. The latter was oligomerized on a 18mer ssDNA, to provide a single but fully functional LexA$_{Pa}$ binding site. A high-nanomolar dissociation constant has been obtained by fitting the data using a bimolecular binding model (K_D^{App} = 390 ± 50 nM).

at 18 min (Figure 4D). Notably, Cory and coworkers reported full filamentation proficiency for RecA$_{Ec}$F203A, which aligns with our findings at the endpoint of the curve.[37] The slower kinetics observed for RecA$_{Pa}$F202A in our study were likely not captured in Cory et al.'s experimental procedure, which focused only on endpoint measurements.

The influence of M201A and F202A mutations on RecA$_{Pa}$ ability to stimulate LexA$_{Pa}$ self-cleavage was evaluated by monitoring the autoproteolysis of FlAsH-LexA$_{Pa}$^{CTD}. Each RecA$_{Pa}$ variant was pre-incubated with ssDNA and ATPγS long enough to guarantee full filamentation before addition to the LexA self-cleavage reporter construct. The relative LexA autoproteolysis activity was calculated after 80-min of incubation (Figure S5B). RecA$_{Pa}$M201A displayed a partial ($\sim$30%) reduction in LexA$_{Pa}$ co-protease activity compared to the wild type, while the F202A mutation completely abrogated this activity (Figure 4D). This confirms the key role of Phe202 in LexA$_{Pa}$ engagement and, at the same time, shows that Met201 has a non-negligible effect on its binding.

DISCUSSION

In this work, we solved the structure of the main regulative players of the SOS response (RecA and LexA) in *P. aeruginosa*, a relevant human pathogen whose DNA-damage response still requires thorough understanding.

The structures of LexA$_{Pa}$ C-terminal autoproteolytic domain (Figure 1), activated RecA$_{Pa}$ (i.e., complexed with ssDNA and ATPγS, referred to as RecA$_{Pa}$*; Figure 2), and their complex (RecA$_{Pa}$*-LexA$_{Pa}$S125A; Figure 3) were obtained by X-ray crystallography and cryo-electron microscopy, respectively.

While writing our manuscript, Cory and co-workers published a preprint manuscript describing the complex of *E. coli* RecA and full-length LexA.[37] Besides supporting our main results, their structure, together with previous structural studies,[36] offered the opportunity to highlight peculiarities of the SOS components and activation complex here disclosed.

RecA$_{Pa}$ has been structurally investigated in complex with ssDNA and ATPγS, showing an extended helical assembly, which is kept unaltered upon LexA$_{Pa}$ binding. RecA$_{Pa}$ sequence is highly homologous to RecA$_{Ec}$, with the highest differences affecting the very C-terminal tail (residues 330–346 in *P. aeruginosa*; Figure S1C). In both species this region has a high percentage of acidic residues and is likely very flexible, thus it is not visible in previous (e.g.,: PDB: 7JY6 and 3CMW)[46,47] and in our structures. Superposition of RecA$_{Pa}$* structure to RecA$_{Ec}$* (PDB: 7JY6)[46] revealed a very high global and local structural similarity, with conservation of the main residues defining the binding sites for ATPγS and ssDNA.

The repressor LexA$_{Pa}$, whose C-terminal autoproteolytic domain structure has been determined in this study at 1.70 Å resolution, displays a dimeric assembly with a fully resolved cleavable loop in the open conformation in the crystal packing. When compared to the LexA$_{Ec}$ homolog, the full-length LexA$_{Pa}$ displays unique features such as a shorter C-terminal tail and a longer linker region between its CTD and NTD. Both these regions might contribute to notable binding sites of regulators or

putative inhibitors, given their proximity to the cleavage loop. For instance, these areas of LexA$_{Ec}$ are involved in the binding of both phage GIL01 gp7 LexA-modulating protein[58] and recently developed anti-LexA nanobodies.[30]

The cryo-EM structure of *P. aeruginosa* SOS complex revealed that the full-length LexA$_{Pa}$S125A decorates RecA$_{Pa}$* non-stoichiometrically. This was clearly confirmed by our data processing, as all the attempts made to reconstruct the complex using helical refinement, imposing RecA$_{Pa}$* helical symmetry, failed. On the other hand, using single particle reconstruction and homogeneous refinement, we obtained a clear and well-defined density (Figure 3B), corresponding to a dimer of LexA$_{Pa}$S125A C-terminal domains into the groove of a six-member turn of RecA$_{Pa}$* (Figures 3C and 3D). This result agrees with the *E. coli* complex recently described by Cory and coworkers,[37] while it diverges from the previous RecA$_{Ec}$*-LexA$_{Ec}$^{CTD} complex structure (PDB: 8GMS),[36] where LexA autoproteolytic CTD was fully decorating the RecA$_{Ec}$* filament and followed its helical symmetry. The symmetrical architecture observed by Gao and colleagues is likely due to the absence of LexA$_{Ec}$ NTD domains, which cannot exert any steric hindrance on adjacent LexA binding sites.

Full-length LexA$_{Pa}$ binding mainly entails the engagement of three consecutive RecA$_{Pa}$ protomers (chains G, H, and I; Figures 3F–3I), as shown by the extension of the buried surface areas: 993 Å^2 are buried on LexA$_{Pa}$^{A} (14.4% of its total surface) at the interface with these three chains (Figure 3K–3M). Among these three, the central one (chain H in our complex) contributes most and protrudes with Phe202 (located on the L2 loop) in a hydrophobic pocket that is formed only upon closure of LexA$_{Pa}$ cleavable loop toward its catalytic crevice (Figures 1F and 3H). Several polar and non-polar interactions can stabilize the two binding partners. The upstream RecA$_{Pa}$ protomer (chain G; toward the 3′ terminus of ssDNA) contacts the same LexA$_{Pa}$ chain by hydrophobic/van der Waals interactions (involving Met201), while the downstream RecA$_{Pa}$ protomer (chain I; toward the 5′ terminus of ssDNA) could define multiple polar contacts with LexA$_{Pa}$^{A} (Figures 3G–3I). Last, a fourth RecA$_{Pa}$ protomer (chain J) is placed at a distance compatible with further electrostatic interactions with both chains of the LexA$_{Pa}$ dimer (Figure 3J). However, the contribution of chain J to the binding of LexA$_{Pa}$ is likely very limited, as noticed by Cory and colleagues for *E. coli*.[37] The centrality of RecA$_{Pa}$ Phe202 and, to a lesser extent, Met201 in LexA$_{Pa}$ binding was confirmed by mutational experiments: RecA$_{Pa}$ F202A mutant loses completely the ability to trigger LexA$_{Pa}$ autoproteolysis while the M201A mutant partially compromises the same co-protease activity (Figure 4D).

The protein surface and key determinants of the RecA*-LexA interaction are highly conserved between *E. coli* and *P. aeruginosa*. A peculiar difference consists in the conformation of the LexA repressor NTD domain. Indeed, in both complexes it partially occupies the groove of RecA* but it results poorly defined and more peripheral in the *P. aeruginosa* structure. Such differences are most likely due to a roughly twice longer linker connecting the NTD and CTD domains of LexA$_{Pa}$ (eleven versus five amino acids of the *E. coli* homolog). Such a long spacer introduces higher flexibility between the two domains

of LexA$_{Pa}$ and it might prevent the formation of stable interactions by the NTD domain with RecA$_{Pa}$* oligomers.

The structures presented here unravel that the main determinants of the activation process reside in the CTD domain, supporting the significance of the RecA$_{Pa}$*-LexA$_{Pa}$^{CTD} binding measurements performed *in vitro* on recombinant purified species (Figures 4A–4C). Dissociation constants of RecA$_{Pa}$ to ssDNA (to form RecA$_{Pa}$*) and RecA$_{Pa}$* to LexA$_{Pa}$^{CTD}, evaluated by dedicated FP-based assays, fall in the mid (K_D^{App} = 82 ± 34 nM) and high nanomolar range (K_D^{App} = 390 ± 50 nM), respectively. Although it might be affected by the oligonucleotide length used in the assay, the affinity of RecA$_{Pa}$ toward ssDNA is in the expected range. The binding constant between the components of the activation complex results in a remarkable agreement with the previously determined one for a full-length *E. coli* LexA S119A with its cognate RecA* (360 nM).[51]

Our experimental data strongly supports the most accepted model proposed for the activation of the SOS response (Figure 4E). In the absence of "*SOS*" *stimuli*, the equilibrium between the closed and the open conformations of LexA cleavage loop largely favors the uncleavable one, leaving LexA intact and capable of repressing the SOS genes. After exposure to stressors, the resulting DNA damage promotes RecA* nucleoprotein filaments assembly, providing a molecular surface able to selectively bind LexA in the closed conformation and free from dsDNA (as SOS box DNA is known to hamper RecA* binding).[18] This binding event alters the equilibrium between LexA conformations in favor of the cleavable one, while co-catalyzing the LexA autocleavage.

This notion finds clear support in the structural analysis of the complex, where only the closed state of LexA fits the binding region of RecA* oligomers, and the cleavable loop is engaged in extensive interactions with recombinase protomers by residues distributed both upstream and downstream the scissile peptide bond.

Since LexA cleavable loop contributes to defining the hydrophobic pocket that hosts RecA key phenylalanine, upon LexA autoproteolysis the binding site for RecA* is divided among the cleavage products. It is likely that this allows their dissociation from RecA*. This model agrees with previous observations that LexA^{CTD} affinity for RecA* remains comparable to that of full-length LexA, provided that the N-terminal truncation leaves intact the initial structured region of the CTD (starting at residue G75 in *E. coli*, G81 in *P. aeruginosa*).[59]

A deep understanding of the SOS response at the molecular level is of great significance for both general and medical microbiology. Indeed, this stress response pathway to DNA damage is widely recognized as one of the main drivers of the evolution of antibiotic resistance and a master regulator of several disease-related phenomena. On the other hand, recent works have pinpointed significant inter-species differences in this conserved and long-studied pathway, underlining that it still has hidden aspects, especially in non-model organisms.

The structures of the essential SOS components and their activation complex in the *P. aeruginosa* pathogen, as presented here, along with the recent models revealed for the *E. coli* bacterial model, have successfully addressed a gap that persisted for over three decades in basic research. These findings have uncovered pivotal elements, crucial for designing innovative strategies to combat bacterial pathogens, focusing on anti-evolutionary and antivirulence approaches.

Limitations of the study

Limitations of this study include the inability to resolve the N-terminal, DNA-binding domain of LexA$_{Pa}$ in the cryo-EM map of RecA$_{Pa}$*-LexA$_{Pa}$. As discussed previously, this might be due to the intrinsic flexibility of this domain and its minor role in the complex formation.

One potential limitation of this study can be identified in the stabilization of the RecA$_{Pa}$*-LexA$_{Pa}$ by chemical crosslinking, a step introduced to enrich the population of LexA$_{Pa}$-decorated complexes. However, the fact that two other independent studies obtained coherent results employing slightly different molecular systems indicates that our reconstruction provided a *bona fide* structure of the complex.

Data on RecA$_{Pa}$ affinity for ssDNA and ATPγS and on the K_D between RecA$_{Pa}$* and LexA$_{Pa}$ present some limitations, since multiple and likely interwoven equilibria occur in solution.

RESOURCE AVAILABILITY

Lead contact

Further information and requests for resources and reagents should be directed to and will be fulfilled by the lead contact, Laura Cendron (laura.cendron@unipd.it).

Materials availability

All constructs used in this study are available upon reasonable request from the lead contact. All constructs were sequence-verified via Sanger sequencing.

Data and code availability

- The data generated in this study are available upon reasonable request from the lead contact. X-ray and cryo-EM structures and maps generated in this study have been deposited on the PDB and EMDB databases and are publicly available as of the date of publication. Accession numbers are listed in the key resources table.
- This paper does not report original code.
- Any additional information required to reanalyze the data reported in this paper is available from the lead contact upon request.

AUTHOR CONTRIBUTIONS

F.V.: conceptualization, investigation, formal analysis, data curation, methodology, writing—original draft, writing—review and editing. S.D.F.: conceptualization, investigation, formal analysis, data curation, methodology, writing—original draft, writing—review and editing. M.G.: conceptualization, investigation, formal

analysis, data curation, writing—original draft. S.H.: methodology, formal analysis, data curation. M.C.: investigation, formal analysis, methodology. R.M.: investigation, formal analysis. C.C.: methodology, formal analysis, data curation. A.G.: methodology, data curation. F.F.: supervision, data curation, writing—review and editing. L.M.: investigation, methodology, formal analysis. A.J.: methodology, formal analysis, data curation. L.C.: conceptualization, investigation, methodology, writing—original draft, writing—review and editing, project administration, resources, supervision, validation.

DECLARATION OF INTERESTS

The authors declare no competing interests.

STAR★METHODS

Detailed methods are provided in the online version of this paper and include the following:

- KEY RESOURCES TABLE
- EXPERIMENTAL MODEL AND SUBJECT DETAILS
- METHOD DETAILS
  - Molecular cloning and site-directed mutagenesis
  - Recombinant protein expression and purification
  - SDS-PAGE-based RecA$_{Pa}$*-mediated LexA$_{Pa}$ autoproteolysis assay
  - LexA$_{Pa}^{CTD}$G91D crystallization
  - X-Ray structure determination
  - Isolation of multi-protein complexes for Cryo-EM studies
  - Cryo-EM data collection
  - Image processing and 3D reconstruction
  - Model building, refinement and structural analysis
  - Fluorescence polarization-based studies
- QUANTIFICATION AND STATISTICAL ANALYSIS

SUPPLEMENTAL INFORMATION

Supplemental information can be found online at https://doi.org/10.1016/j.isci.2024.111726.

REFERENCES

1. Murray, C.J.L., Ikuta, K.S., Sharara, F., Swetschinski, L., Robles Aguilar, G., Gray, A., Han, C., Bisignano, C., Rao, P., Wool, E., et al. (2022). Global burden of bacterial antimicrobial resistance in 2019: a systematic analysis. Lancet *399*, 629–655. https://doi.org/10.1016/S0140-6736(21)02724-0.

2. Tacconelli, E., Carrara, E., Savoldi, A., Harbarth, S., Mendelson, M., Monnet, D.L., Pulcini, C., Kahlmeter, G., Kluytmans, J., Carmeli, Y., et al. (2018). Discovery, research, and development of new antibiotics: the WHO priority list of antibiotic-resistant bacteria and tuberculosis. Lancet Infect. Dis. *18*, 318–327. https://doi.org/10.1016/S1473-3099(17)30753-3.

3. Pang, Z., Raudonis, R., Glick, B.R., Lin, T.-J., and Cheng, Z. (2019). Antibiotic resistance in Pseudomonas aeruginosa: mechanisms and alternative therapeutic strategies. Biotechnol. Adv. *37*, 177–192. https://doi.org/10.1016/j.biotechadv.2018.11.013.

4. Rice, L.B. (2008). Federal Funding for the Study of Antimicrobial Resistance in Nosocomial Pathogens: No ESKAPE. J. Infect. Dis. *197*, 1079–1081. https://doi.org/10.1086/533452.

5. Liao, C., Huang, X., Wang, Q., Yao, D., and Lu, W. (2022). Virulence Factors of Pseudomonas Aeruginosa and Antivirulence Strategies to Combat Its Drug Resistance. Front. Cell. Infect. Microbiol. *12*, 926758. https://doi.org/10.3389/fcimb.2022.926758.

6. Qin, S., Xiao, W., Zhou, C., Pu, Q., Deng, X., Lan, L., Liang, H., Song, X., and Wu, M. (2022). Pseudomonas aeruginosa: pathogenesis, virulence factors, antibiotic resistance, interaction with host, technology advances and emerging therapeutics. Signal Transduct. Targeted Ther. *7*, 199. https://doi.org/10.1038/s41392-022-01056-1.

7. Podlesek, Z., and Žgur Bertok, D. (2020). The DNA Damage Inducible SOS Response Is a Key Player in the Generation of Bacterial Persister Cells and Population Wide Tolerance. Front. Microbiol. *11*, 1785. https://doi.org/10.3389/fmicb.2020.01785.

8. Mulani, M.S., Kamble, E.E., Kumkar, S.N., Tawre, M.S., and Pardesi, K.R. (2019). Emerging Strategies to Combat ESKAPE Pathogens in the Era of Antimicrobial Resistance: A Review. Front. Microbiol. *10*, 539. https://doi.org/10.3389/fmicb.2019.00539.

9. Merrikh, H., and Kohli, R.M. (2020). Targeting evolution to inhibit antibiotic resistance. FEBS J. *287*, 4341–4353. https://doi.org/10.1111/febs.15370.

10. Culyba, M.J., Mo, C.Y., and Kohli, R.M. (2015). Targets for Combating the Evolution of Acquired Antibiotic Resistance. Biochemistry *54*, 3573–3582. https://doi.org/10.1021/acs.biochem.5b00109.

11. Mühlen, S., and Dersch, P. (2016). Anti-virulence Strategies to Target Bacterial Infections. Curr. Top. Microbiol. Immunol. *398*, 147–183. https://doi.org/10.1007/82_2015_490.

12. Gotoh, H., Kasaraneni, N., Devineni, N., Dallo, S.F., and Weitao, T. (2010). SOS involvement in stress-inducible biofilm formation. Biofouling *26*, 603–611. https://doi.org/10.1080/08927014.2010.501895.

13. Lima-Noronha, M.A., Fonseca, D.L.H., Oliveira, R.S., Freitas, R.R., Park, J.H., and Galhardo, R.S. (2022). Sending out an SOS - the bacterial DNA damage response. Genet. Mol. Biol. *45*, e20220107. https://doi.org/10.1590/1678-4685-gmb-2022-0107.

14. Galhardo, R.S., Do, R., Yamada, M., Friedberg, E.C., Hastings, P.J., Nohmi, T., and Rosenberg, S.M. (2009). DinB Upregulation Is the Sole Role of the SOS Response in Stress-Induced Mutagenesis in Escherichia coli. Genetics *182*, 55–68. https://doi.org/10.1534/genetics.109.100735.

15. Pacheco, A.R., and Sperandio, V. (2012). Shiga toxin in enterohemorrhagic E.coli: regulation and novel anti-virulence strategies. Front. Cell. Infect. Microbiol. *2*, 81. https://doi.org/10.3389/fcimb.2012.00081.

16. Dawan, J., and Ahn, J. (2022). Bacterial Stress Responses as Potential Targets in Overcoming Antibiotic Resistance. Microorganisms *10*, 1385. https://doi.org/10.3390/microorganisms10071385.

17. Zhang, A.P.P., Pigli, Y.Z., and Rice, P.A. (2010). Structure of the LexA-DNA complex and implications for SOS box measurement. Nature *466*, 883–886. https://doi.org/10.1038/nature09200.

18. Butala, M., Klose, D., Hodnik, V., Rems, A., Podlesek, Z., Klare, J.P., Anderluh, G., Busby, S.J.W., Steinhoff, H.-J., and Žgur-Bertok, D. (2011). Interconversion between bound and free conformations of LexA orchestrates the bacterial SOS response. Nucleic Acids Res. *39*, 6546–6557. https://doi.org/10.1093/nar/gkr265.

19. Luo, Y., Pfuetzner, R.A., Mosimann, S., Paetzel, M., Frey, E.A., Cherney, M., Kim, B., Little, J.W., and Strynadka, N.C. (2001). Crystal Structure of LexA: A Conformational Switch for Regulation of Self-Cleavage. Cell *106*, 585–594. https://doi.org/10.1016/S0092-8674(01)00479-2.

20. Mo, C.Y., Birdwell, L.D., and Kohli, R.M. (2014). Specificity Determinants for Autoproteolysis of LexA, a Key Regulator of Bacterial SOS Mutagenesis. Biochemistry *53*, 3158–3168. https://doi.org/10.1021/bi500026e.

21. Culyba, M.J., Kubiak, J.M., Mo, C.Y., Goulian, M., and Kohli, R.M. (2018). Non-equilibrium repressor binding kinetics link DNA damage dose to transcriptional timing within the SOS gene network. PLoS Genet. *14*, e1007405. https://doi.org/10.1371/journal.pgen.1007405.

22. Simmons, L.A., Foti, J.J., Cohen, S.E., and Walker, G.C. (2008). The SOS Regulatory Network. EcoSal Plus *3*, 10–128. https://doi.org/10.1128/ecosalplus.5.4.3.

23. Mérida-Floriano, A., Rowe, W.P.M., and Casadesús, J. (2021). Genome-Wide Identification and Expression Analysis of SOS Response Genes in

Salmonella enterica Serovar Typhimurium. Cells *10*, 943. https://doi.org/10.3390/cells10040943.

24. Cirz, R.T., O'Neill, B.M., Hammond, J.A., Head, S.R., and Romesberg, F.E. (2006). Defining the Pseudomonas aeruginosa SOS Response and Its Role in the Global Response to the Antibiotic Ciprofloxacin. J. Bacteriol. *188*, 7101–7110. https://doi.org/10.1128/JB.00807-06.

25. Erill, I., Campoy, S., and Barbé, J. (2007). Aeons of distress: an evolutionary perspective on the bacterial SOS response. FEMS Microbiol. Rev. *31*, 637–656. https://doi.org/10.1111/j.1574-6976.2007.00082.x.

26. Jatsenko, T., Sidorenko, J., Saumaa, S., and Kivisaar, M. (2017). DNA Polymerases ImuC and DinB Are Involved in DNA Alkylation Damage Tolerance in Pseudomonas aeruginosa and Pseudomonas putida. PLoS One *12*, e0170719. https://doi.org/10.1371/journal.pone.0170719.

27. Luján, A.M., Moyano, A.J., Martino, R.A., Feliziani, S., Urretavizcaya, M., and Smania, A.M. (2019). ImuB and ImuC contribute to UV-induced mutagenesis as part of the SOS regulon in Pseudomonas aeruginosa. Environ. Mol. Mutagen. *60*, em.22290. https://doi.org/10.1002/em.22290.

28. Fujii, S., and Fuchs, R.P. (2020). A Comprehensive View of Translesion Synthesis in Escherichia coli. Microbiol. Mol. Biol. Rev. *84*, e00002-20. https://doi.org/10.1128/MMBR.00002-20.

29. Lu, T.K., and Collins, J.J. (2009). Engineered bacteriophage targeting gene networks as adjuvants for antibiotic therapy. Proc. Natl. Acad. Sci. USA *106*, 4629–4634. https://doi.org/10.1073/pnas.0800442106.

30. Maso, L., Vascon, F., Chinellato, M., Goormaghtigh, F., Bellio, P., Campagnaro, E., Van Melderen, L., Ruzzene, M., Pardon, E., Angelini, A., et al. (2022). Nanobodies targeting LexA autocleavage disclose a novel suppression strategy of SOS-response pathway. Structure *30*, 1479–1493. https://doi.org/10.1016/j.str.2022.09.004.

31. Mo, C.Y., Culyba, M.J., Selwood, T., Kubiak, J.M., Hostetler, Z.M., Jurewicz, A.J., Keller, P.M., Pope, A.J., Quinn, A., Schneck, J., et al. (2018). Inhibitors of LexA Autoproteolysis and the Bacterial SOS Response Discovered by an Academic–Industry Partnership. ACS Infect. Dis. *4*, 349–359. https://doi.org/10.1021/acsinfecdis.7b00122.

32. Bellio, P., Di Pietro, L., Mancini, A., Piovano, M., Nicoletti, M., Brisdelli, F., Tondi, D., Cendron, L., Franceschini, N., Amicosante, G., et al. (2017). SOS response in bacteria: Inhibitory activity of lichen secondary metabolites against Escherichia coli RecA protein. Phytomedicine *29*, 11–18. https://doi.org/10.1016/j.phymed.2017.04.001.

33. Yakimov, A., Pobegalov, G., Bakhlanova, I., Khodorkovskii, M., Petukhov, M., and Baitin, D. (2017). Blocking the RecA activity and SOS-response in bacteria with a short α-helical peptide. Nucleic Acids Res. *45*, 9788–9796. https://doi.org/10.1093/nar/gkx687.

34. Barreto, K., Bharathikumar, V.M., Ricardo, A., DeCoteau, J.F., Luo, Y., and Geyer, C.R. (2009). A Genetic Screen for Isolating "Lariat" Peptide Inhibitors of Protein Function. Chem. Biol. *16*, 1148–1157. https://doi.org/10.1016/j.chembiol.2009.10.012.

35. Selwood, T., Larsen, B.J., Mo, C.Y., Culyba, M.J., Hostetler, Z.M., Kohli, R.M., Reitz, A.B., and Baugh, S.D.P. (2018). Advancement of the 5-Amino-1-(Carbamoylmethyl)-1H-1,2,3-Triazole-4-Carboxamide Scaffold to Disarm the Bacterial SOS Response. Front. Microbiol. *9*, 2961. https://doi.org/10.3389/fmicb.2018.02961.

36. Gao, B., Liang, L., Su, L., Wen, A., Zhou, C., and Feng, Y. (2023). Structural basis for regulation of SOS response in bacteria. Proc. Natl. Acad. Sci. USA *120*, e2217493120. https://doi.org/10.1073/pnas.2217493120.

37. Cory, M.B., Li, A., Hurley, C.M., Carman, P.J., Pumroy, R.A., Hostetler, Z.M., Perez, R.M., Venkatesh, Y., Li, X., Gupta, K., et al. (2024). The LexA–RecA* structure reveals a cryptic lock-and-key mechanism for SOS activation. Nat. Struct. Mol. Biol. *31*, 1522–1531. https://doi.org/10.1038/s41594-024-01317-3.

38. Penterman, J., Singh, P.K., and Walker, G.C. (2014). Biological Cost of Pyocin Production during the SOS Response in Pseudomonas aeruginosa. J. Bacteriol. *196*, 3351–3359. https://doi.org/10.1128/JB.01889-14.

39. Jiao, H., Li, F., Wang, T., Yam, J.K.H., Yang, L., and Liang, H. (2021). The Pyocin Regulator PrtR Regulates Virulence Expression of Pseudomonas aeruginosa by Modulation of Gac/Rsm System and c-di-GMP Signaling Pathway. Infect. Immun. *89*, e00602-20. https://doi.org/10.1128/IAI.00602-20.

40. Fan, Z., Chen, H., Li, M., Pan, X., Fu, W., Ren, H., Chen, R., Bai, F., Jin, Y., Cheng, Z., et al. (2019). Pseudomonas aeruginosa Polynucleotide Phosphorylase Contributes to Ciprofloxacin Resistance by Regulating PrtR. Front. Microbiol. *10*, 1762. https://doi.org/10.3389/fmicb.2019.01762.

41. McFarland, K.A., Dolben, E.L., LeRoux, M., Kambara, T.K., Ramsey, K.M., Kirkpatrick, R.L., Mougous, J.D., Hogan, D.A., and Dove, S.L. (2015). A self-lysis pathway that enhances the virulence of a pathogenic bacterium. Proc. Natl. Acad. Sci. USA *112*, 8433–8438. https://doi.org/10.1073/pnas.1506299112.

42. Mohana-Borges, R., Pacheco, A.B., Sousa, F.J., Foguel, D., Almeida, D.F., and Silva, J.L. (2000). LexA Repressor Forms Stable Dimers in Solution. J. Biol. Chem. *275*, 4708–4712. https://doi.org/10.1074/jbc.275.7.4708.

43. Engilberge, S., Riobé, F., Di Pietro, S., Lassalle, L., Coquelle, N., Arnaud, C.-A., Pitrat, D., Mulatier, J.-C., Madern, D., Breyton, C., et al. (2017). Crystallophore: a versatile lanthanide complex for protein crystallography combining nucleating effects, phasing properties, and luminescence. Chem. Sci. *8*, 5909–5917. https://doi.org/10.1039/C7SC00758B.

44. Engilberge, S., Wagner, T., Santoni, G., Breyton, C., Shima, S., Franzetti, B., Riobé, F., Maury, O., and Girard, E. (2019). Protein crystal structure determination with the crystallophore, a nucleating and phasing agent. J. Appl. Crystallogr. *52*, 722–731. https://doi.org/10.1107/S1600576719006381.

45. Agirre, J., Atanasova, M., Bagdonas, H., Ballard, C.B., Baslé, A., Beilsten-Edmands, J., Borges, R.J., Brown, D.G., Burgos-Mármol, J.J., Berrisford, J.M., et al. (2023). The CCP4 suite: integrative software for macromolecular crystallography. Acta Crystallogr. D Struct. Biol. *79*, 449–461. https://doi.org/10.1107/S2059798323003595.

46. Yang, H., Zhou, C., Dhar, A., and Pavletich, N.P. (2020). Mechanism of strand exchange from RecA–DNA synaptic and D-loop structures. Nature *586*, 801–806. https://doi.org/10.1038/s41586-020-2820-9.

47. Chen, Z., Yang, H., and Pavletich, N.P. (2008). Mechanism of homologous recombination from the RecA–ssDNA/dsDNA structures. Nature *453*, 489–494. https://doi.org/10.1038/nature06971.

48. Bell, J.C., and Kowalczykowski, S.C. (2016). RecA: Regulation and Mechanism of a Molecular Search Engine. Trends Biochem. Sci. *41*, 491–507. https://doi.org/10.1016/j.tibs.2016.04.002.

49. VanLoock, M.S., Yu, X., Yang, S., Lai, A.L., Low, C., Campbell, M.J., and Egelman, E.H. (2003). ATP-Mediated Conformational Changes in the RecA Filament. Structure *11*, 187–196. https://doi.org/10.1016/S0969-2126(03)00003-0.

50. Lee, A.M., Wigle, T.J., and Singleton, S.F. (2007). A complementary pair of rapid molecular screening assays for RecA activities. Anal. Biochem. *367*, 247–258. https://doi.org/10.1016/j.ab.2007.04.021.

51. Cory, M.B., Li, A., Hurley, C.M., Hostetler, Z.M., Venkatesh, Y., Jones, C.M., Petersson, E.J., and Kohli, R.M. (2022). Engineered RecA Constructs Reveal the Minimal SOS Activation Complex. Biochemistry *61*, 2884–2896. https://doi.org/10.1021/acs.biochem.2c00505.

52. Kowalczykowski, S.C. (1986). Interaction of RecA protein with a photoaffinity analog of ATP, 8-azido-ATP: determination of nucleotide cofactor binding parameters and of the relationship between ATP binding and ATP hydrolysis. Biochemistry *25*, 5872–5881. https://doi.org/10.1021/bi00368a006.

53. Story, R.M., and Steitz, T.A. (1992). Structure of the recA protein–ADP complex. Nature *355*, 374–376. https://doi.org/10.1038/355374a0.

54. Mirshad, J.K., and Kowalczykowski, S.C. (2003). Biochemical Characterization of a Mutant RecA Protein Altered in DNA-Binding Loop 1. Biochemistry *42*, 5945–5954. https://doi.org/10.1021/bi027233i.

55. Malkov, V.A., and Camerini-Otero, R.D. (1995). Photocross-links between Single-stranded DNA and Escherichia coli RecA Protein Map to Loops L1

(Amino Acid Residues 157-164) and L2 (Amino Acid Residues 195-209). J. Biol. Chem. *270*, 30230–30233. https://doi.org/10.1074/jbc.270.50.30230.

56. Gardner, R.V., Voloshin, O.N., and Camerini-Otero, R.D. (1995). The Identification of the Single-Stranded DNA-Binding Domain of the Escherichia coli RecA Protein. Eur. J. Biochem. *233*, 419–425. https://doi.org/10.1111/j.1432-1033.1995.419_2.x.

57. Shibata, T., Ikawa, S., Iwasaki, W., Sasanuma, H., Masai, H., and Hirota, K. (2024). Homology recognition without double-stranded DNA-strand separation in D-loop formation by RecA. Nucleic Acids Res. *52*, 2565–2577. https://doi.org/10.1093/nar/gkad1260.

58. Caveney, N.A., Pavlin, A., Caballero, G., Bahun, M., Hodnik, V., de Castro, L., Fornelos, N., Butala, M., and Strynadka, N.C.J. (2019). Structural Insights into Bacteriophage GIL01 gp7 Inhibition of Host LexA Repressor. Structure *27*, 1094–1102. https://doi.org/10.1016/j.str.2019.03.019.

59. Hostetler, Z.M., Cory, M.B., Jones, C.M., Petersson, E.J., and Kohli, R.M. (2020). The Kinetic and Molecular Basis for the Interaction of LexA and Activated RecA Revealed by a Fluorescent Amino Acid Probe. ACS Chem. Biol. *15*, 1127–1133. https://doi.org/10.1021/acschembio.9b00886.

60. Giese, K.C., Michalowski, C.B., and Little, J.W. (2008). RecA-Dependent Cleavage of LexA Dimers. J. Mol. Biol. *377*, 148–161. https://doi.org/10.1016/j.jmb.2007.12.025.

61. Evans, P.R. (2011). An introduction to data reduction: space-group determination, scaling and intensity statistics. Acta Crystallogr. D Biol. Crystallogr. *67*, 282–292. https://doi.org/10.1107/S090744491003982X.

62. Vagin, A., and Teplyakov, A. (2010). Molecular replacement with MOLREP. Acta Crystallogr. D Biol. Crystallogr. *66*, 22–25. https://doi.org/10.1107/S0907444909042589.

63. Waterhouse, A., Bertoni, M., Bienert, S., Studer, G., Tauriello, G., Gumienny, R., Heer, F.T., De Beer, T.A.P., Rempfer, C., Bordoli, L., et al. (2018). SWISS-MODEL: Homology modelling of protein structures and complexes. Nucleic Acids Res. *46*, W296–W303. https://doi.org/10.1093/nar/gky427.

64. Emsley, P., Lohkamp, B., Scott, W.G., and Cowtan, K. (2010). Features and development of Coot. Acta Crystallogr. D Biol. Crystallogr. *66*, 486–501. https://doi.org/10.1107/S0907444910007493.

65. Murshudov, G.N., Skubák, P., Lebedev, A.A., Pannu, N.S., Steiner, R.A., Nicholls, R.A., Winn, M.D., Long, F., and Vagin, A.A. (2011). REFMAC5 for the refinement of macromolecular crystal structures. Acta Crystallogr. Sect. D Biol. Crystallogr. *67*, 355–367. https://doi.org/10.1107/S0907444911001314.

66. Winn, M.D., Ballard, C.C., Cowtan, K.D., Dodson, E.J., Emsley, P., Evans, P.R., Keegan, R.M., Krissinel, E.B., Leslie, A.G.W., McCoy, A., et al. (2011). Overview of the CCP4 suite and current developments. Acta Crystallogr. D Biol. Crystallogr. *67*, 235–242. https://doi.org/10.1107/S0907444910045749.

67. Kandiah, E., Giraud, T., de Maria Antolinos, A., Dobias, F., Effantin, G., Flot, D., Hons, M., Schoehn, G., Susini, J., Svensson, O., et al. (2019). CM01: a facility for cryo-electron microscopy at the European Synchrotron. Acta Crystallogr. D Struct. Biol. *75*, 528–535. https://doi.org/10.1107/S2059798319006880.

68. Zheng, S.Q., Palovcak, E., Armache, J.-P., Verba, K.A., Cheng, Y., and Agard, D.A. (2017). MotionCor2: anisotropic correction of beam-induced

motion for improved cryo-electron microscopy. Nat. Methods *14*, 331–332. https://doi.org/10.1038/nmeth.4193.

69. Zhang, K. (2016). Gctf: Real-time CTF determination and correction. J. Struct. Biol. *193*, 1–12. https://doi.org/10.1016/j.jsb.2015.11.003.

70. Zivanov, J., Nakane, T., Forsberg, B.O., Kimanius, D., Hagen, W.J., Lindahl, E., and Scheres, S.H. (2018). New tools for automated high-resolution cryo-EM structure determination in RELION-3. Elife *7*, e42166. https://doi.org/10.7554/eLife.42166.

71. Punjani, A., Rubinstein, J.L., Fleet, D.J., and Brubaker, M.A. (2017). cryoSPARC: algorithms for rapid unsupervised cryo-EM structure determination. Nat. Methods *14*, 290–296. https://doi.org/10.1038/nmeth.4169.

72. Kimanius, D., Dong, L., Sharov, G., Nakane, T., and Scheres, S.H.W. (2021). New tools for automated cryo-EM single-particle analysis in RELION-4.0. Biochem. J. *478*, 4169–4185. https://doi.org/10.1042/BCJ20210708.

73. Jakobi, A.J., Wilmanns, M., and Sachse, C. (2017). Model-based local density sharpening of cryo-EM maps. Elife *6*, e27131. https://doi.org/10.7554/eLife.27131.

74. Bharadwaj, A., and Jakobi, A.J. (2022). Electron scattering properties of biological macromolecules and their use for cryo-EM map sharpening. Faraday Discuss *240*, 168–183. https://doi.org/10.1039/D2FD00078D.

75. Afonine, P.V., Grosse-Kunstleve, R.W., Echols, N., Headd, J.J., Moriarty, N.W., Mustyakimov, M., Terwilliger, T.C., Urzhumtsev, A., Zwart, P.H., and Adams, P.D. (2012). Towards automated crystallographic structure refinement with phenix.refine. Acta Crystallogr. D Biol. Crystallogr. *68*, 352–367. https://doi.org/10.1107/S0907444912001308.

76. Kelley, L.A., Mezulis, S., Yates, C.M., Wass, M.N., and Sternberg, M.J.E. (2015). The Phyre2 web portal for protein modeling, prediction and analysis. Nat. Protoc. *10*, 845–858. https://doi.org/10.1038/nprot.2015.053.

77. Afonine, P.V., Poon, B.K., Read, R.J., Sobolev, O.V., Terwilliger, T.C., Urzhumtsev, A., and Adams, P.D. (2018). Real-space refinement in PHENIX for cryo-EM and crystallography. Acta Crystallogr. D Struct. Biol. *74*, 531–544. https://doi.org/10.1107/S2059798318006551.

78. Krissinel, E., and Henrick, K. (2007). Inference of Macromolecular Assemblies from Crystalline State. J. Mol. Biol. *372*, 774–797. https://doi.org/10.1016/j.jmb.2007.05.022.

79. Adasme, M.F., Linnemann, K.L., Bolz, S.N., Kaiser, F., Salentin, S., Haupt, V.J., and Schroeder, M. (2021). PLIP 2021: expanding the scope of the protein–ligand interaction profiler to DNA and RNA. Nucleic Acids Res. *49*, W530–W534. https://doi.org/10.1093/nar/gkab294.

80. Jurrus, E., Engel, D., Star, K., Monson, K., Brandi, J., Felberg, L.E., Brookes, D.H., Wilson, L., Chen, J., Liles, K., et al. (2018). Improvements to the APBS biomolecular solvation software suite. Protein Sci. *27*, 112–128. https://doi.org/10.1002/pro.3280.

81. Stefan, M.I., and Le Novère, N. (2013). Cooperative Binding. PLoS Comput. Biol. *9*, 2–7. https://doi.org/10.1371/journal.pcbi.1003106.

82. Jarmoskaite, I., Alsadhan, I., Vaidyanathan, P.P., and Herschlag, D. (2020). How to measure and evaluate binding affinities. Elife *9*, e57264. https://doi.org/10.7554/ELIFE.57264.

83. Gesztelyi, R., Zsuga, J., Kemeny-Beke, A., Varga, B., Juhasz, B., and Tosaki, A. (2012). The Hill equation and the origin of quantitative pharmacology. Arch. Hist. Exact Sci. *66*, 427–438. https://doi.org/10.1007/s00407-012-0098-5.

STAR★METHODS

KEY RESOURCES TABLE

REAGENT or RESOURCE	SOURCE	IDENTIFIER
Bacterial and virus strains		
Escherichia coli BL21(DE3)	New England Biolabs	Cat#C2527H
Pseudomonas aeruginosa	ATCC	ATCC 27853
Chemicals, peptides, and recombinant proteins		
FlAsH-EDT2	Cayman Chemical	Cat#20704; CAS: 212118-77-9
ATPγS	Jena Bioscience	Cat#NU-406; CAS: 93839-89-5
SUMO Protease	Invitrogen	Cat#12588-018
Disuccinimidyl suberate (DSS)	Thermo Scientific	Cat#21655; CAS: 68528-80-3
Tb-Xo4 Crystallophore N°1	Molecular Dimensions (Polyvalan)	Cat#MD2-82; CAS: 2101838-38-2
Critical commercial assays		
LMB, PACT Premier and JCSG Plus crystallization kits	Molecular Dimensions	Cat#MD1-123, MD1-98, MD1-29, MD1-37
QuikChange II Site-Directed Mutagenesis Kit	Agilent Technologies	Cat#200518
GenElute Bacterial Genomic DNA Kit	Merck	Cat#NA2100
pColiExpress I Bacterial expression Kit	Canvax	Cat#BE001
Expresso T7 SUMO Cloning and Expression System	Lucigen	Cat#MA108
Expresso T7 Cloning and Expression System	Lucigen	Cat#MA101
Deposited data		
Crystal structure of LexA$_{Pa}^{CTD}$G91D	This paper	PDB: 8B0V
Cryo-EM structure of RecA$_{Pa}$*	This paper	PDB: 8S70; EMDB: 19761
Cryo-EM structure of RecA$_{Pa}$*-LexA$_{Pa}$S125A	This paper	PDB: 8S7G; EMDB: 19771
Oligonucleotides		
SKBT25-18mer (5′- GCGTGTGTGGTGGTGTGC-3′)	Giese et al., 2008[59]	N/A
FAM-32mer (5′- CCATCCGCAA AAATGACCTCTTATCAAAAGGA -3′	Lee et al., 2007[49]	N/A
72mer oligo(dT) (5′-T$_{72}$ -3′)	This paper	N/A
Primers used in molecular cloning and mutagenesis are reported in Table S3	This paper	N/A
Recombinant DNA		
pColiXP-RecA$_{Pa}$	This paper	N/A
pColiXP-RecA$_{Pa}$M201A	This paper	N/A
pColiXP-RecA$_{Pa}$F202A	This paper	N/A
pColiXP-LexA$_{Pa}^{CTD}$	This paper	N/A
pColiXP-LexA$_{Pa}^{CTD}$G91D	This paper	N/A
pETite-LexA$_{Pa}$	This paper	N/A
pETite-LexA$_{Pa}$S125A	This paper	N/A
pETite-SUMO-4Cys-LexA$_{Pa}^{CTD}$	This paper	N/A
pETite-SUMO-4Cys-LexA$_{Pa}^{CTD}$S125A	This paper	N/A
Software and algorithms		
CCP4i2	Winn et al., 2011[60]	https://www.ccp4.ac.uk/
Aimless	Evans, 2011[61]	https://www.ccp4.ac.uk/html/aimless.html
Molrep	Vagin & Teplyakov, 2010[62]	https://www.ccp4.ac.uk/html/molrep.html
Coot	Emsley et al., 2010[63]	https://www2.mrc-lmb.cam.ac.uk/personal/pemsley/coot/
Refmac5	Murshudov et al., 2011[64]	https://www.ccp4.ac.uk/html/refmac5.html
MotionCor2	Zheng et al., 2017[65]	https://emcore.ucsf.edu/ucsf-software

(Continued on next page)

Continued

REAGENT or RESOURCE	SOURCE	IDENTIFIER
Gctf	Zhang et al., 2016[66]	
RELION 3.1.1	Zivanov et al., 2018[67]	https://relion.readthedocs.io/en/release-3.0/
CryoSPARC v4.2.1	Punjani et al., 2017[68]	https://cryosparc.com/
RELION 4.0.0	Kimanius et al., 2021[69]	https://relion.readthedocs.io/en/release-4.0/
LocScale2	Jakobi et al., 2017[70]	https://gitlab.tudelft.nl/aj-lab/locscale
SwissModel	Waterhouse et al., 2018[71]	https://swissmodel.expasy.org/
Phyre2	Kelley et al., 2015[72]	http://www.sbg.bio.ic.ac.uk/~phyre2/html/page.cgi?id=index
Phenix	Afonine et al., 2018[73]	https://phenix-online.org/
UCSF Chimera	RBVI, University of California	https://www.cgl.ucsf.edu/chimera/
PyMol v2.0	Schrödinger LLC	https://pymol.org/2/
Other		
HisTrap Excel His tag protein purification columns (1 mL and 5 mL)	Cytiva	Cat#17371205; Cat#17371206
HiLoad Superdex 75 26/60 PG column	GE Healthcare	Cat#28-9893-34
Superdex 200 10/300 GL column	GE Healthcare	Cat#17-5175-01
Quantifoil R 1.2/1.3 Cu 300 mesh holey carbon grids	Quantifoil	Cat#N1-C14nCu30
Nunc™ 384-Well ShallowWell Standard Height Black	ThermoFisher Scientific	Cat#264705

EXPERIMENTAL MODEL AND SUBJECT DETAILS

P. aeruginosa ATCC 27853 was cultured for genome extraction in LB medium at 37°C. *E. coli* BL21(DE3) cells were used for protein expression and cultured in LB medium supplemented with the opportune antibiotic, as further detailed in the following paragraphs.

METHOD DETAILS

Molecular cloning and site-directed mutagenesis

The genomic DNA of *P. aeruginosa* ATCC 27853 was purified from an overnight liquid culture using the GenElute Bacterial Genomic DNA Kit (Merck) according to manufacturer's instructions. The coding sequences of *P. aeruginosa* RecA (RecA$_{Pa}$) and LexA C-terminal domain (LexA$_{Pa}^{CTD}$) were PCR-amplified from *P. aeruginosa* ATCC 27853 gDNA using primers RecA_Pa_pColi.For/Rev and LexA_CTD_Pa_pColi.For/Rev, respectively (Table S3) and cloned in the pColiExpressI plasmid vector (Canvax) by ligation-independent cloning following manufacturers' instructions. The obtained plasmids were named pColiXP-RecA$_{Pa}$ and pColiXP-LexA$_{Pa}^{CTD}$. The coding sequence of *P. aeruginosa* full-length LexA (LexA$_{Pa}$) and TetraCys-tagged LexA$_{Pa}^{CTD}$ were amplified from the genomic DNA using primers LexA_Pa.For/Rev and LexA_Pa_CTD_4Cys.For/Rev (Table S3) and cloned in pETite C-His Kan vector and pETite N-His SUMO Kan Vector (Lucigen), respectively, via ligation-independent cloning following manufacturer's instructions. The obtained plasmid vectors will be referred to as pETite-LexA$_{Pa}$ and pETite-SUMO-4Cys-LexA$_{Pa}^{CTD}$.

The three plasmids encoding LexA$_{Pa}$ variants were used as templates to introduce inactivating mutations either altering LexA$_{Pa}$ cleavable loop (G91D) or its catalytic site (S125A), using the QuikChange Site-Directed Mutagenesis kit (Agilent Technologies) and mutagenic primers listed in Table S3 pColiXP-RecA$_{Pa}$ was used as template to introduce the M201A and F202A mutations on RecA$_{Pa}$.

All generated plasmids were verified by Sanger sequencing.

Recombinant protein expression and purification
RecA$_{Pa}$ and its mutants

N-terminal His-tagged *P. aeruginosa* Recombinase A (RecA$_{Pa}$) was expressed in *E. coli* BL21(DE3) cells, transformed with pColiXP-RecA$_{Pa}$ and grown in LB broth supplemented with 100 μg/mL ampicillin. Protein overexpression was induced by adding 1 mM isopropyl-β-D-thiogalactoside (IPTG) to the bacterial culture in the late exponential growth phase (OD$_{600}$ 0.6–0.8) and was carried out overnight at room temperature under vigorous shaking (180 rpm). Cells were harvested by centrifugation and resuspended in buffer R_A (10 mM HEPES, 300 mM NaCl, 10% v/v Glycerol, 20 mM Imidazole, pH 8.0) supplemented with 1X Protease Inhibitors Cocktail (SERVA) and a tip of spatula of DNAse I (Sigma Aldrich). Bacterial cells lysis was performed by sonication. Cell debris were removed by centrifugation and the lysate soluble fraction was loaded on a 5 mL HisTrap Excel IMAC column (Cytiva). His-tagged RecA$_{Pa}$ was eluted after extensive buffer R_A washes, by linearly raising the imidazole concentration in the eluent from 20 mM to 500 mM in 3 column volumes. IMAC fractions showing RecA$_{Pa}$ as the main protein component in SDS-PAGE analysis were pooled together,

concentrated using a Vivaspin Turbo Ultrafiltration unit (10 kDa MWCO; Sartorius) and buffer-exchanged in 10 mM HEPES, 300 mM NaCl, 10% Glycerol, 1 mM MgCl$_2$, 1 mM dithiothreitol (DTT), pH 7.0, by a HiTrap Desalting column (Cytiva) before storage at −80°C for future usage in *in vitro* assays. Since the N-terminal 6xHisTag did not interfere with RecA$_{Pa}$ assembly on ssDNA and with RecA$_{Pa}$*-mediated LexA$_{Pa}$ self-cleavage, it was not removed after protein purification.

The M201A and F202A mutants of RecA$_{Pa}$ were expressed and purified following the same protocol reported for the wild-type protein.

LexA$_{Pa}$ variants

N-terminal His-tagged LexA$_{Pa}$, either wild-type or S125A catalytically inactive mutant (LexA$_{Pa}$S125A), and C-terminal His-tagged LexA$_{Pa}$ C-terminal domain, either wild-type or G91D uncleavable mutant (LexA$_{Pa}$^{CTD}G91D), were expressed in *E. coli* BL21(DE3) cells, transformed with pETite-LexA$_{Pa}$ (S125A) and pColiXP-LexA$_{Pa}$^{CTD} (G91D), respectively. Cells were grown in LB broth supplemented with 50 μg/mL kanamycin or 100 μg/mL ampicillin, respectively. Protein overexpression was induced by adding 1 mM isopropyl-β-D-thiogalactoside (IPTG) to bacterial cultures in the late exponential growth phase (OD$_{600}$ 0.6–0.8) and was carried out overnight at room temperature under vigorous shaking (180 rpm). Cells were harvested by centrifugation and resuspended in buffer L_A (20 mM Tris-HCl, 150 mM NaCl, 10% v/v Glycerol, pH 7.5) supplemented with 20 mM Imidazole, 1X Protease Inhibitors Cocktail (SERVA), 500 U of benzonase nuclease (Merck) and 1.5 mM MgCl$_2$. Bacterial cells were lysed by sonication and the crude lysate was incubated 30 min at 4°C to allow benzonase-mediated DNA digestion. The supernatant was cleared by centrifugation and loaded on a 1 mL HisTrap Excel IMAC column (Cytiva). After thoroughly washing the resin with buffer L_A and with 20 mM imidazole in buffer L_A, His-tagged LexA$_{Pa}$ variants were eluted by linearly raising the imidazole concentration in the eluent from 20 mM to 500 mM in 10 column volumes. IMAC fractions showing LexA$_{Pa}$S125A as the main protein component by SDS-PAGE analysis were pooled together, concentrated using a Vivaspin Turbo Ultrafiltration unit (5 kDa MWCO; Sartorius) and buffer-exchanged to buffer L_A by a HiPrep 26/10 desalting column (Cytiva) before storage at −80°C. IMAC fractions containing mostly pure 6His-LexA$_{Pa}$^{CTD} G91D, as evidenced by SDS-PAGE analysis, were pooled together, concentrated and further purified by size-exclusion chromatography on a HiLoad Superdex 75 26/60 PG column (Cytiva) equilibrated in 20 mM tris-HCl pH 7.6, 150 mM NaCl, 5% v/v glycerol. The affinity tag was cleaved from 6His-LexA$_{Pa}$^{CTD} G91D by incubating the purified protein overnight at 4°C with recombinant TEV protease (LexA:TEV ratio of 20:1, w/w), 0.4 mM DTT, 0.15 mM EDTA and 0.01% v/v NP-40. The following day, the mixture was diluted twice with buffer L_A to reduce DTT and EDTA concentration and then loaded on a 1 mL HisTrap Excel IMAC column, recovering the flowthrough that contains LexA$_{Pa}$^{CTD} G91D without 6xHisTag. This sample was then buffer exchanged to 20 mM tris-HCl pH 7.6, 150 mM NaCl, 5% v/v glycerol and concentrated to 11.5 mg/mL before storage at −80°C for protein crystallization.

FlAsH-LexA$_{Pa}$^{CTD} and its mutants

N-terminal His-SUMO-4Cys-tagged *P. aeruginosa* LexA C-terminal domain (either wild type or its S125A inactive variant) was expressed in *E. coli* BL21(DE3) cells, transformed with pETite-SUMO-LexA$_{Pa}$^{CTD} (wt or S125A) and grown in LB broth supplemented with 50 μg/mL kanamycin. Protein overexpression was induced by adding 1 mM isopropyl-β-D-thiogalactoside (IPTG) to the bacterial culture in the late exponential growth phase (OD$_{600}$ 0.6–0.8) and was carried out overnight at room temperature under vigorous shaking (180 rpm). Cells were harvested by centrifugation and resuspended in buffer FL_A (20 mM Tris-HCl, 150 mM NaCl, 10% v/v Glycerol, 0.1 mM DTT, pH 7.5) supplemented with 20 mM Imidazole and 1X Protease Inhibitors Cocktail (SERVA). Bacterial cells lysis was performed by sonication. Cell debris were removed by centrifugation and the lysate soluble fraction was loaded on a 1 mL HisTrap Excel IMAC column (Cytiva). After extensively washing the column with buffer FL_A and with 20 mM imidazole in buffer FL_A, 6His-SUMO-4Cys-LexA$_{Pa}$^{CTD} was eluted by linearly raising the imidazole concentration in the eluent from 20 mM to 500 mM in 10 column volumes. IMAC fractions showing 6His-SUMO-4Cys-LexA$_{Pa}$^{CTD} as the main protein component by SDS-PAGE analysis were pooled together, diluted three times in buffer FL_A and supplemented by 1 mM DTT, 1 mM EDTA, 0.1% v/v NP-40, and an excess of Expresso Sumo Protease (Lucigen). Following a 2-h incubation at room temperature with gentle shaking, 100 μM FlAsH-EDT$_2$ was added to the reaction mix and the incubation was prolonged overnight at 4°C in the dark. The mixture was then concentrated using a Vivaspin Turbo Ultrafiltration unit (5 kDa MWCO; Sartorius) and buffer-exchanged to 20 mM tris-HCl, 150 mM NaCl, 10% v/v Glycerol, pH 7.5 by a PD-10 desalting column (Cytiva). To remove 6His-SUMO fragments and uncleaved protein constructs from the final sample, the mixture was passed through a 1 mL HisTrap Excel IMAC column (Cytiva) and the flowthrough was recovered. FlAsH-LexA$_{Pa}$^{CTD} was stored at −80°C for future usage in *in vitro* assays.

SDS-PAGE-based RecA$_{Pa}$*-mediated LexA$_{Pa}$ autoproteolysis assay

RecA$_{Pa}$ was co-incubated 1h at 37°C with SKBT25-18mer[60] ssDNA ([RecA$_{Pa}$]:[18mer ssDNA] = 3.5:1) and a molar excess (1 mM) of ATPγS. To test the RecA$_{Pa}$*-induced autoproteolytic activity of purified LexA$_{Pa}$ variants, 1 μM of each variant was incubated with 1 μM RecA$_{Pa}$* at 37°C. 30 mM HEPES, 150 mM NaCl, pH 7.1 was used as the reaction buffer. The reaction was stopped at different time points by adding Laemmli sample buffer and incubating the samples 5 min at 95°C before loading them on Bis-Tris-SDS 4–20% polyacrylamide gels (SurePAGE, GenScript).

The gels were stained by Coomassie blue and protein bands were quantified using ImageJ. For each lane, the intensity of the bands corresponding to either uncleaved LexA$_{Pa}$ or its autoproteolysis products were first normalized on the RecA$_{Pa}$ band to screen for possible loading errors, and then on the band of uncleaved LexA$_{Pa}$ at time 0.

LexA$_{Pa}$^{CTD}G91D crystallization

11.5 mg/mL LexA$_{Pa}$^{CTD} G91D underwent large-scale crystallization trials by the sitting-drop isothermal vapor diffusion method. 0.4 μL drops were produced mixing an equal volume of protein and precipitant solutions (PACT, LMB and JCSG-plus crystallization kits; Molecular Dimensions) by an Oryx8 dispensing robot (Douglas Instruments) and incubated at 293 K. The best crystals grew in buffers 1–23, 2–9 and 2–11 of the PACT premier crystallization trial kit and were further optimized by the addition of 5 mM Tb-Xo4 (Crystallophore 1, Polyvalan)[43,44] to the protein solution as nucleating agent. Crystals were cryo-protected by adding 30% v/v PEG 400 to the mother liquor before freezing in liquid nitrogen for shipment to the synchrotron facility.

X-Ray structure determination

X-ray diffraction experiments of protein crystals were performed at the ID30B beamline of the European Synchrotron Radiation Facility (ESRF, Grenoble, France). Best LexA$_{Pa}$^{CTD} G91D diffracting crystals were obtained in PACT 1–23 precipitant buffer (0.2 M CaCl$_2$·2H$_2$O, 0.1 M MES pH 6.0, 20% w/v PEG 6000). Collected data were analyzed by the available automated processing pipelines for space group determination and reflections indexing. Data reduction was performed by Aimless via the CCP4i2 interface.[61] Molecular replacement was carried out by Molrep,[62] using a homology model of LexA$_{Pa}$^{CTD}G91D generated by SwissModel[63] using PDB 1JHF as a template. The protein model was adjusted by manual and automated structure refinement, using Coot[64] and Refmac5[65] via the CCP4i2 interface.[66] The LexA$_{Pa}$^{CTD}G91D dimer was reconstructed in Pymol v2.3.5 applying the crystallographic symmetry operator.

Isolation of multi-protein complexes for Cryo-EM studies

165 μM RecA$_{Pa}$ was incubated over the weekend on ice with 13 μM 72mer oligo(dT) ssDNA and 1 mM ATPγS to induce RecA$_{Pa}$ oligomerization on ssDNA. The sample was diluted three times, either in 10 mM HEPES, pH 7.1, 150 mM NaCl (*RecA$_{Pa}$** sample) or by adding LexA$_{Pa}$S125A to a final concentration of 53 μM and incubated 2h at 4°C (*RecA$_{Pa}$*-LexA$_{Pa}$S125A* sample). Samples underwent protein crosslinking by adding 2.5 mM disuccinimidyl suberate (DSS; 5% v/v DMSO) and incubating overnight at 4°C under gentle agitation. Reactions were quenched by adding 100 mM Tris (pH 7.0) for 2h at room temperature. Protein pellet was removed by centrifugation before loading the mixture on a Superdex 200 10/300 GL size-exclusion chromatography column (Cytiva), pre-equilibrated with 20 mM Tris-HCl, pH 7.5, 150 mM NaCl.

As revealed by electron microscopy preliminary observation of the different samples recovered, the helical nucleoprotein complexes were eluted with the void volume of the column.

Samples were concentrated by Vivaspin centrifugal devices (MWCO 50 kDa; Sartorius) before deposition on grids for cryogenic electron microscopy (Cryo-EM).

Cryo-EM data collection

3 μL of freshly purified RecA$_{Pa}$* complex (2.3 mg/mL) were applied to a glow discharged Quantifoil R 1.2/1.3 Cu300 holey carbon grid. Excess sample was blotted away, and the grid was plunge-frozen into liquid ethane using a Mark IV Vitrobot (1.0 s blot time, 10°C, 100% humidity) at the Florence Center for Electron Nanoscopy (Dept. of Chemistry, University of Florence, Italy). The grids were imaged on the 300 kV Titan Krios microscope (Thermo Fisher Scientific) of the CM01 facility of the ESRF[67] with a K2 direct electron detector camera (Gatan, USA) operated in counting mode and at a pixel size of 0.827 Å per pixel. A total of 8711 movies were collected with 50 frames each, a fractional exposure of 0.98 e$^-$/Å^2 per frame and using a defocus range from −0.8 to −2.0 μm.

3 μL of RecA$_{Pa}$*-LexA$_{Pa}$S125A were applied to a glow-discharged Quantifoil R 1.2/1.3 copper 300-mesh holey carbon grids. The grid was blotted and plunge-frozen as reported above. The grids were imaged on the 300 kV Titan Krios microscope (Thermo Fisher Scientific) of the CM01 facility of the ESRF[67] with a K3 direct electron camera (Gatan, USA) operated in counting mode and at a pixel size of 0.84 Å per pixel. A total of 7882 movies were collected with 54 frames each, a fractional exposure of 1.02 e$^-$/Å^2 per frame and using a defocus range from −1 to −2.0 μm in 0.2 μm steps. The exposure rate was 16.9 e$^-$/pixel/sec for a total nominal exposure of 55.08 e$^-$/Å^2.

Image processing and 3D reconstruction

For both datasets, motion correction was performed by Motioncor2[68] and parameters of the contrast transfer function (CTF) were estimated by Gctf.[69] For the RecA$_{Pa}$* dataset, 6543 micrographs were selected for the analysis. A small set of filaments was manually traced (Figure S2) from a subset of micrographs to obtain initial 2D class averages for use as templates for reference-based auto-picking in RELION 3.1.1 [70]. 609530 segments were automatically picked and extracted to a box size of 384 X 384 pixels with an overlap of 85% and imported into CryoSPARC v4.2.1 [71]. Following 2D classification, 202842 segments were selected and used for 3D refinement, using helical parameters already reported for the RecA* homolog from *E. coli* as starting values (i.e., helical twist = 59° and rise = 15.5 Å).[36]

Particles were further subjected to local and global CTF refinement yielding a consensus map at 4.2 Å overall resolution (Figure S3) with final helical parameters as reported in Table S2.

For RecA$_{Pa}$*-LexA$_{Pa}$S125A initial attempts of automatic picking failed. Therefore 104800 tubes were manually picked and extracted to a box size of 384 X 384 pixels with an overlap of 85% in RELION 4.0.0 [72]. After several rounds of 2D classification, 561719 particles were used as input for the generation of a 3D initial model with C1 symmetry using a spherical mask of 350 Å, in

RELION 4.0.0. After import into CryoSPARC v4.2.1 [71] and heterogeneous refinement, 438072 particles were selected for a further round of homogeneous refinement. Following two rounds of 3D classification, first using a spherical mask of radius 50 Å centered on LexA density, and then a structure-based mask encompassing the LexA$_{Pa}$ density, were used to select 164165 particles, corresponding to the classes presenting additional density in the RecA$_{Pa}$* groove which we ascribed to LexA$_{Pa}$. After local and global CTF refinement, homogeneous refinement led to a consensus map at 3.4 Å overall resolution (Figure S4).

Local amplitude scaling was performed using the model-free implementation of local sharpening with reference profiles in LocScale2[73,74] with a cubic averaging window of 25 Å edge length and starting from the unfiltered half maps. The locally scaled map was used for display purposes (Figures 2A, 2B, 3A, 3B, S3, and S4); atomic model refinement and model-map FSC calculations were done using the original half maps.

Model building, refinement and structural analysis

A homology model for the atomic structure of monomeric RecA$_{Pa}$ was generated by SwissModel[63] using PDB 2REB (monomeric *E. coli* RecA) as a template. The model was fitted into a zone corresponding to a single RecA$_{Pa}$ monomer in the cryo-EM map. Then the full oligomer was reconstructed by applying the helical symmetry parameters using UCSF Chimera. The ssDNA poly(dT) chain, ATPγS and Mg^{2+} ions were built and fitted using Coot.[64] The resulting model was refined by iterative cycles of automated real space refinement in Phenix.[75] For RecA$_{Pa}$*-LexA$_{Pa}$S125A, our structure of RecA$_{Pa}$* was used as the starting model. LexA$_{Pa}$^{CTD} in the cleavable conformation (i.e., with the cleavable loop closed) was modeled by Phyre2 web server in the "one-to-one threading" mode,[76] using LexA$_{Ec}$^{CTD} from PDB 8GMS as the template. The closed cleavable loop was then grafted on chain A of LexA$_{Pa}$^{CTD} G91D X-ray structure and the S125A mutation was introduced by PyMol v2.3.5. RecA$_{Pa}$* and the model of LexA$_{Pa}$^{CTD} dimer were fitted into the respective densities in the map and refined by automatic and manual real-space refinement methods using Phenix in the default mode[77] and Coot,[64] respectively. Analysis of protein-protein and protein-ligand interactions was performed by PDBePISA (https://www.ebi.ac.uk/pdbe/pisa/)[78] and PLIP (https://plip-tool.biotec.tu-dresden.de/plip-web/plip/index).[79] Surface electrostatic potential maps were generated by the APBS-PDB2PQR webserver (https://server.poissonboltzmann.org/),[80] simulating an environment with pH 7.5 and 0.1 M NaCl.

Fluorescence polarization-based studies

Fluorescence polarization (FP) was used as the biophysical readout to observe and quantify the binding of RecA$_{Pa}$ to ssDNA and LexA$_{Pa}$ to RecA$_{Pa}$*. All the FP assays reported below were performed in Nunc 384-Well Black plates and by an EnVision Multimode plate reader equipped with opportune filters. 30 mM HEPES pH 7.1, 150 mM NaCl, 1 mM MgCl$_2$ was used as the reaction buffer. Each sample was produced at least in triplicate.

To determine the apparent affinity of RecA$_{Pa}$ for ssDNA and ATPγS, a 5′-Carboxyfluoresceinated 32-mer oligonucleotide (FAM-32mer; Table S3) was used as "scaffold".[50,51]

In the former experiment, 10 nM FAM-32mer ssDNA was incubated with different concentrations of RecA$_{Pa}$ and an excess of ATPγS (1 mM) for 30 min at 37°C before reading the FP signal. FP data measured without RecA$_{Pa}$ and at 17 µM RecA$_{Pa}$ were considered as "0% oligomerization" and "100% oligomerization", respectively, and used to normalize all the collected data, thus deriving the fraction of RecA$_{Pa}$-bound ssDNA in each sample. The RecA$_{Pa}$-bound fraction (F_B) of FAM-32mer ssDNA was plotted against RecA$_{Pa}$ concentration and experimental data were best-fitted in GraphPad Prism 8 by a Hill equation (Equation 1, where h is the Hill coefficient).[81–83]

$$F_B = \frac{[RecA]^h}{[RecA]^h + (K_A)^h} = \frac{[RecA]^h}{[RecA]^h + K_D^{App}} \qquad \text{(Equation 1)}$$

Conversely, to estimate RecA$_{Pa}$ apparent affinity for ATPγS, 10 nM FAM-32mer ssDNA and 1 µM RecA$_{Pa}$ were incubated with different concentrations of ATPγS for 30 min at 37°C before reading the FP signal. FP data measured without ATPγS and at 10 mM ATPγS were considered as "0% oligomerization" and "100% oligomerization", respectively, and used to normalize all the collected data. The RecA$_{Pa}$-bound fraction of FAM-32mer ssDNA was plotted against ATPγS concentration and experimental data were best-fitted in GraphPad Prism 8 by a Hill equation (Equation 2).

$$F_B = \frac{[ATP\gamma S]^h}{[ATP\gamma S]^h + (K_A)^h} = \frac{[ATP\gamma S]^h}{[ATP\gamma S]^h + K_D^{App}} \qquad \text{(Equation 2)}$$

To determine the apparent affinity of LexA$_{Pa}$ to RecA$_{Pa}$*, FlAsH-LexA$_{Pa}$^{CTD}S125A was used as the fluorescent probe at a fixed concentration of 0.1 µM. RecA$_{Pa}$ was pre-activated with SKBT25-18mer ssDNA and ATPγS and then added at different concentrations. Following a 30 min incubation at 37°C, the FP signal was measured. FP data measured without RecA$_{Pa}$* (0% binding) and at 10 µM RecA$_{Pa}$* (100% binding) were used to normalize all the data and obtain the RecA$_{Pa}$*-bound fraction of FlAsH-LexA$_{Pa}$^{CTD} S125A. Normalized data were best-fitted in GraphPad Prism 8 by a single binding site model.

To investigate the effect of the M201A and F202A mutations on RecA$_{Pa}$ and its interaction with LexA$_{Pa}$, the two mutants and the wild-type variant were submitted to FP-based analysis of oligomerization on ssDNA and FlAsH-LexA$_{Pa}$^{CTD} autoproteolysis induction.

In the former experiment, 10 nM FAM-32mer ssDNA was incubated with 1 μM RecA$_{Pa}$ (either wt, M201A or F202A) and 10 μM ATPγS. Control reactions included only FAM-32mer and ATPγS. The FP signal was monitored for 60 min at 37°C. The relative oligomerization activity was calculated at 18 min of incubation, as wild-type RecA$_{Pa}$ required this time to reach full oligomerization (as evidenced by a plateau in the FP traces; Equation 3).

To assess the LexA$_{Pa}$ co-proteolysis activity of RecA$_{Pa}$ variants, each of them was pre-activated with SKBT25-18mer ssDNA ([RecA]:[18mer] = 3.5:1) and ATPγS (1 mM) for 1.5 h at 37°C, and then added to FlAsH-LexA$_{Pa}^{CTD}$ in equimolar ratio (1 μM). Control reactions included only FlAsH-LexA$_{Pa}^{CTD}$. The FP signal was monitored for 80 min at 37°C and the relative co-proteolysis activity was calculated on the last timepoint according to Equation 3.

$$\text{Relative activity} = \frac{FP^{Mutant}_{Time = x} - FP^{Ctrl}_{Time = x}}{FP^{WT}_{Time = x} - FP^{Ctrl}_{Time = x}} \qquad \text{(Equation 3)}$$

QUANTIFICATION AND STATISTICAL ANALYSIS

The number of replicates performed for each experiment is reported in the corresponding method paragraph. Averages and errors are reported in the tables, figures or captions. Curve fitting was performed using GraphPad Prism v8.00, according to the models indicated in the respective method paragraphs.